

# Controlling the Dynamics of Microstructure Formation in Mixed-Matrix Polymeric-Particle Membranes

Thesis by  
Rachel R. Ford

In Partial Fulfillment of the Requirements for  
the degree of  
Doctor of Philosophy

CALIFORNIA INSTITUTE OF TECHNOLOGY  
Pasadena, California

2021  
(Defended September 11, 2020)

© 2021

Rachel R. Ford

ORCID: 0000-0001-9844-1557

## ACKNOWLEDGEMENTS

I have so many people to thank for helping me get here; I'm sure any compilation I construct will be insufficient. Above all, I thank God for everything that led me to Caltech and everything that has come of it. I do not think there could exist a better combination of graduate advisors for me than Prof. Julie Kornfield and Prof. Mamadou Diallo. I have so appreciated their guidance, teaching, and support through the program. I would also like to thank my committee for their critiques, suggestions, and support.

For sparking my interest in chemistry in high school, for teaching an extra class after normal school hours, for mentoring me and encouraging me in the years since, I thank Mrs. Debra Scott.

For teaching me organic chemistry, for admitting me into his research group at the University of Florida, and for being a mentor to me through undergrad and beyond, I thank Prof. Ken Wagener. Your support, encouragement, and guidance have been integral to my success. "You never leave the group; you simply change locations."

For advising me as an undergraduate researcher, for giving me an opportunity to expand my understanding and application of chemistry to the pharmaceutical field, and for impressing upon me the importance of literature searches extending prior to 1980, I thank Prof. Ken Sloan.

For being my mentor, for encouraging me to design and test my own experiments, for putting up with my many mistakes, for counseling me throughout my career path, and for admitting me as the first member of the Schulz Sub-Group, I thank (now-professor) Michael Schulz.

For their comradery, support, and advice (& occasional commiseration), I thank the Kornfield Group. I have truly enjoyed the friendship and mentorship, as well as the opportunity to mentor, throughout the program. You all have helped me become a better communicator and a better scientist. I'd especially like to thank Kate Davies, Abigail McCann, and Christine Jary for your heroic efforts keeping our group running and managing Dr. Kornfield's hectic schedule.

I would like to thank the Resnick Sustainability Institute for funding and for the supportive community that came along with it. I would especially like to thank Neil Fromer and Heidi Rusina for their encouragement and counsel.

I am grateful for the many opportunities I have had to conduct experiments, present research, and learn more about membranes and scattering at different facilities around the world. In particular, I would like to thank William Heller, Ken Littrell, Luke Heroux, Kunlun Hong, Peter Bonnesen, and the late Michael Agamalian at Oak Ridge National Laboratory; as well as Paul Butler, Yun Liu, and Markus Bleuel at the NIST Center for Neutron Research, for their advice and assistance in conducting neutron scattering experiments. I would also like to thank everyone involved in the National School on Neutron and X-ray Scattering at Argonne National Laboratory and at Oak Ridge. Additionally, I thank the organizing committees for the US-Korea Nano Forum and the US-Africa Forum on Nanotechnology Convergence, for the opportunities they provided to connect with researchers around the world.

I would also like to thank Calvary Presbyterian Church. You truly became my church family, offering untold support through the highs and lows of grad school. I would especially like to thank my “adoptive” family, the von Bibras, as well as Huw and Rachel Christopher.

Finally, I cannot express deeply enough my gratitude for my parents and my family. Without their patience, their counsel, their love, and their support throughout my life, but especially during graduate school, I would not have made it to this point. Mom and Dad, I am so very thankful to have you as my parents.



## ABSTRACT

Polymer membranes are increasingly important in energy generation, water purification, and resource recovery. Control over chemistry, morphology, and mechanical properties gives organic polymers unparalleled advantages for membrane technology—but only if these complementary functions can be married into a cohesive material. Herein I have sought to expand upon the chemical tools for integrating diverse polymers into multifunctional membrane materials, making them easily tunable to various applications. To overcome a fundamental challenge in polymer science—namely, that polymers with different functions often do not mix—the functional polymer is grown *in situ* in a solution containing a preformed scaffold polymer, a method pioneered by co-advisor Mamadou Diallo. The hierarchical structure of the resulting mixed matrix polymeric-particle (M2P2) membrane is governed by the kinetic competition between polymerization and phase separation of the functional polymer from the scaffold polymer. This competition is quenched by immersion in a nonsolvent, which rapidly solidifies the material to trap the metastable structure formed during synthesis.

In my quest to understand how these competing processes interact to inform multifunctional membrane design, I developed a general method for studying transient structure using ultra-small angle neutron scattering (Chapter II), working closely with Kornfield Group alumnus Dr. Joey Kim. I then investigated the synergistic effects of incorporating different functional polymer architectures in M2P2 membranes (Chapter III), working with fellow graduate student Orland Bateman. By combining low-generation dendrimers with randomly hyperbranched oligomers bearing similar chemical functionality, we can systematically tune the characteristic length of domains formed during synthesis. In the final chapter I discuss the main conclusions and describe future directions for understanding structure during processing in M2P2 membranes. My thesis ultimately provides a broadly relevant platform for membrane design and synthesis, one in which the favorable properties of different polymers may be combined to strike a balance between function, stability, and ease of fabrication.



# TABLE OF CONTENTS

Acknowledgements .....	iii
Abstract .....	vi
Table of Contents .....	viii
List of Figures .....	x
List of Tables .....	xii
Abbreviations .....	xiii

## Chapter I: Multifunctional Polymer Materials for Sustainable Technologies

I.1 Mixed-Matrix Polymeric-Particle Membranes .....	1
I.2 <i>In Situ</i> Synthesis: The Solution and the Challenge .....	6
I.3 Objectives .....	7

## Chapter II: Probing Structure Formation in M2P2 Membranes using Neutron Scattering

II.1 Introduction .....	8
II.2 Methods .....	9
II.2.1 Standard synthesis of M2P2 membranes .....	9
II.2.2 Vial-scale experiments .....	10
II.2.3 Preparation of samples for neutron scattering experiments .....	11
II.2.4 Small angle neutron scattering experiments .....	12
II.2.5 Ultra-small angle neutron scattering experiments .....	12
II.2.6 Drop casting of films from USANS samples .....	13
II.2.7 Scanning electron microscopy .....	13
II.2.8 Plotting color scheme .....	14
II.3 Results & Discussion .....	14
II.3.1 Equilibrated structure in final casting solutions .....	14
II.3.2 Time-resolved SANS of M2P2 casting solutions .....	16
II.3.3 Time-resolved USANS .....	17
II.3.4 Effects of solvent deuteration and multiple scattering .....	19
II.3.5 Kinetics of structure formation revealed by USANS .....	24
II.3.6 The “control” was not a control .....	28
II.3.7 Comparison to standard membranes by SEM .....	30
II.4 Summary .....	32



<b>Chapter III: Polymer Architecture Plays a Crucial Role in Microgel Structure Formation</b>	
III.1 Introduction .....	33
III.2 Methods .....	35
III.2.1 Preparation of USANS samples with PAMAM microgels .....	35
III.2.2 Preparation of USANS samples with PAMAM+PEI microgels .....	35
III.2.3 Ultra-small angle neutron scattering experiments .....	35
III.3 Results & Discussion.....	36
III.3.1 Macrophase separation of PAMAM microgels.....	36
III.3.2 Combination of PAMAM and PEI.....	39
III.4 Summary .....	41
<b>Chapter IV: Conclusions and Outlook</b>	
IV.1 Key findings & Implications for Membrane Design.....	42
IV.2 Future Directions: Synthesis of Deuterium-labelled PAMAM Dendrimers .....	42
<b>Appendices</b>	
A. Neutron Scattering Instrumentation & Data Reduction.....	45
A.1 Introduction to Neutron Scattering .....	45
A.2 Data Reduction and Correction.....	47
A.3 Specific Considerations for USANS .....	48
B. Methods of Fitting & Analysis.....	62
B.1 Maximum Likelihood Estimation.....	62
B.2 Determination of $Q_K$ from Kratky plots.....	63
C. Supplementary Data .....	65
C.1 SANS of Individual Polymer Solutions .....	65
C.2 Time-Resolved USANS Patterns.....	66
C.3 Visual evaluation of casting solutions .....	67
<b>Bibliography .....</b>	<b>69</b>

## LIST OF FIGURES

<i>Number &amp; description</i>	<i>Page</i>
<b>I.1</b> Mixed-matrix polymeric-particle (M2P2) membranes .....	2
<b>I.2</b> Third-generation poly(amidoamine) dendrimer.....	3
<b>I.3</b> Phase behavior during M2P2 membrane synthesis.....	7
<b>II.1</b> Drop-cast films from USANS samples .....	13
<b>II.2</b> Global scattering from fully reacted casting solutions.....	15
<b>II.3</b> Time-resolved SANS of casting solutions.....	17
<b>II.4</b> Conventional vs. time-resolved USANS.....	18
<b>II.5</b> Early stages of phase separation .....	21
<b>II.6</b> Effects of contrast in M2P2 solutions.....	22
<b>II.7</b> Late stage of phase separation.....	23
<b>II.8</b> Kratky plots for different concentrations of ECH.....	25
<b>II.9</b> $Q_K$ and $I(Q_K)$ vs. reaction time .....	26
<b>II.10</b> USANS of M2P2 solution without ECH .....	28
<b>II.11</b> Interactions of PEI & PVDF by SANS .....	29
<b>II.12</b> Gelation between PVDF and PEI.....	30
<b>II.13</b> SEM of standard membranes vs. USANS samples .....	31
<b>III.1</b> Effect of precursor architecture on solid M2P2 membranes .....	34
<b>III.2</b> Time-resolved USANS on PAMAM casting solutions .....	36
<b>III.3</b> Effect of ECH on G1-PAMAM scattering profiles.....	38
<b>III.4</b> USANS of solutions with PAMAM+PEI microgels .....	40
<b>III.5</b> $Q_K$ vs. reaction time for PAMAM+PEI sample .....	40
<b>III.6</b> $I(Q^*)$ vs. reaction time for PAMAM casting solutions.....	41
<b>IV.1</b> Published synthesis of protected acrylamide.....	43
<b>IV.2</b> Proposed synthesis of deuterated PAMAMs.....	44
<b>A.1</b> Scattering instruments with different geometries .....	49
<b>A.2</b> USANS patterns include the rocking curve.....	50

<b>A.3</b>	Aerial view of the BT5 USANS instrument at NCNR .....	52
<b>A.4</b>	Scattering of the five “blanks” from the February 2016 experiment.....	53
<b>A.5</b>	Effect of normalization on blanks at the beam center.....	54
<b>A.6</b>	Q-dependent background for 2016 USANS experiments.....	56
<b>A.7</b>	Q-dependent background for 2019 USANS experiments.....	57
<b>A.8</b>	Effect of slit geometry for USANS instruments .....	58
<b>A.9</b>	Raw scattering data for sample HB04D100 compared to $I_{QDB}$ .....	60
<b>A.10</b>	Removal of background-dominated scattering .....	61
<b>B.1</b>	Determination of peak position in Kratky plots.....	64
<b>C.1</b>	SANS of PEI and PVDF solutions .....	66
<b>C.2</b>	Supplementary USANS of casting solutions .....	67
<b>C.3</b>	Progression of color change in polymer mixtures.....	68

## LIST OF TABLES

<i>Number &amp; description</i>	<i>Page</i>
<b>II.1</b> Representative sample compositions .....	12
<b>II.2</b> Power law fit parameters for SANS data.....	15
<b>II.3</b> Power law exponents for $Q_K$ & $I(Q_K)$ , 70–80% D solvent .....	27
<b>II.4</b> Power law exponents for $Q_K$ & $I(Q_K)$ , 100% D solvent.....	27
<b>II.5</b> Solidification of standard membranes vs. USANS samples .....	31
<b>A.1</b> Optimal parameters for incoherent scattering & beam width for Q-dependent background.....	55

## ABBREVIATIONS

**DEUF.** Dendrimer-enhanced ultrafiltration, a process in which a feed solution is treated with a specific ion-chelating dendrimer followed by ultrafiltration to retain the large dendrimer-ion complex. Adjusting the pH of the retentate releases the desired ion and regenerates the dendrimer.

**ECH.** Epichlorohydrin, a reactive and corrosive small molecule used for crosslinking nitrogenous oligomers.

**FWHM.** Full width at half the maximum, a metric to describe broadening of a peak.

**M2P2 membrane.** Mixed-matrix polymeric-particle membrane.

**MLE.** Maximum likelihood estimator (or estimation), a statistical approach to determine the optimal parameters in a model that describes a data set.

**NF.** Nanofiltration, a filtration process utilizing porous membranes with pore sizes ranging from 0.1 – 1 nm in diameter. NF membranes are able to reject viruses, small molecules, and larger multivalent ions.

**NG.** Nucleation and growth, a mechanism of phase separation that results from a system being quenched into the binodal region of the phase diagram.

**NIPS.** Nonsolvent induced phase separation, a process in which a polymer film is solidified by exposure to a solvent that the polymer cannot dissolve in; the polymer then rapidly precipitates.

**NMP.** N-methylpyrrolidone, a polar aprotic organic solvent.

**NMR.** Nuclear magnetic resonance, used to characterize organic compounds.

**PAMAM.** Poly(amidoamine), a dendrimer containing a mixture of amides, primary amines, and tertiary amines with regular two- and three-carbon spacing.

**PEG.** Poly(ethylene glycol), a hydrophilic, fouling-resistant, biocompatible polymer.

**PEI.** Poly(ethyleneimine), a randomly hyperbranched polymer containing a mixture of primary, secondary, and tertiary amines with two-carbon spacing.

**PET.** Poly(ethylene terephthalate), a nonwoven support used for M2P2 membranes to improve mechanical strength in filtration processes.

**PIPS.** Polymerization induced phase separation, a phase separation process in which the growth of a new polymer causes a mixture to become unstable, leading to separation of components into different domains, or phases.

**PVDF.** Poly(vinylidene fluoride), a relatively inert and mechanically robust fluoropolymer synthesized from 1,1-difluoroethylene.

**RO.** Reverse osmosis, a process which utilizes a dense nonporous membrane wherein water molecules dissolve into the membrane and diffuse through, while salt ions are rejected.

**RSD.** Relative standard deviation, a metric for describing error, defined as the quotient of standard deviation over magnitude of the data.

**SANS.** Small-angle neutron scattering, a method that probes structure in the 1 nm to 600 nm size range (*i.e.* nanoscale).

**SD.** Spinodal decomposition, a phase separation mechanism in which an unstable single phase spontaneously and rapidly segregates followed by coarsening at a characteristic lengthscale at later stages. The spinodal regime is given a negative diffusion coefficient.

**SEM.** Scanning electron microscopy.

**S/N.** Signal-to-noise, a means to describe how reliable the data are for an instrument.

**TEP.** Triethylphosphate, a polar aprotic organophosphate solvent.

**TIPS.** Thermally induced phase separation, a process in which a polymer film is solidified using a temperature gradient.

**UF.** Ultrafiltration, a filtration process utilizing porous membranes with pore sizes ranging from 0.1 – 1  $\mu\text{m}$  in diameter. UF membranes can reject small particulates and bacteria.

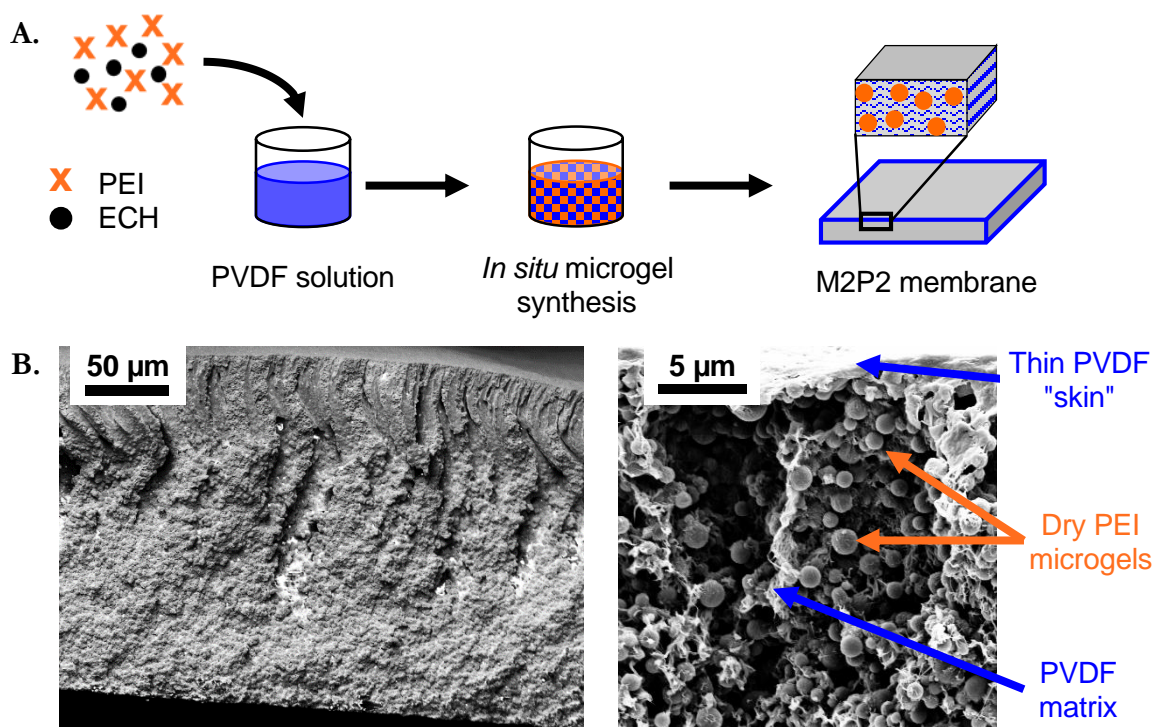
**USANS.** Ultra-small angle neutron scattering, a method that probes structure in the 600 nm to 20  $\mu\text{m}$  size range (*i.e.* microscale).



*Chapter I***MULTIFUNCTIONAL POLYMER MATERIALS  
FOR SUSTAINABLE TECHNOLOGIES****I.1 Mixed-Matrix Polymeric-Particle Membranes**

In recent decades, polymer membranes have been increasingly employed across various industries relevant to sustainability, such as energy generation<sup>1-4</sup>, water purification<sup>5-10</sup>, biological separations<sup>11,12</sup>, and resource recovery<sup>13-18</sup>. Crucial to this effort are mixed-matrix membranes—multicomponent polymer membranes with embedded functional particles. Mixed-matrix membranes allow one to exploit the favorable properties of different components while mitigating their individual drawbacks, striking a balance between function, stability, and ease of fabrication. While mixed-matrix membranes containing inorganic or metallic functional particles are readily fabricated<sup>19</sup>, incorporating functional polymeric particles within a scaffold polymer membrane (of different chemical identity) faces significant challenges due to the often unfavorable thermodynamics of mixing polymers<sup>20</sup>. The Diallo Group overcame these challenges and made considerable advances in the field with their "one-pot" method for the preparation of mixed-matrix membranes with functional polymeric particles<sup>21-25</sup>. Per the Diallo protocol, the functional polymer is grown *in situ* in a solution containing a preformed scaffold polymer; this approach enables the combination of otherwise immiscible polymers to form a cohesive multifunctional material (**Fig. I.1A**). The resultant mixed-matrix polymeric-particle (M2P2) membrane contains unique hierarchical structure owing to the kinetic competition between polymerization and phase separation of the functional polymer from the scaffold polymer, wherein spherical microgel particles are stably anchored in the scaffold matrix (**Fig. I.1B**). This platform for M2P2 membranes provides access to the broad, tunable range of properties afforded by functional polymers, enabling application to a variety of industrial processes.



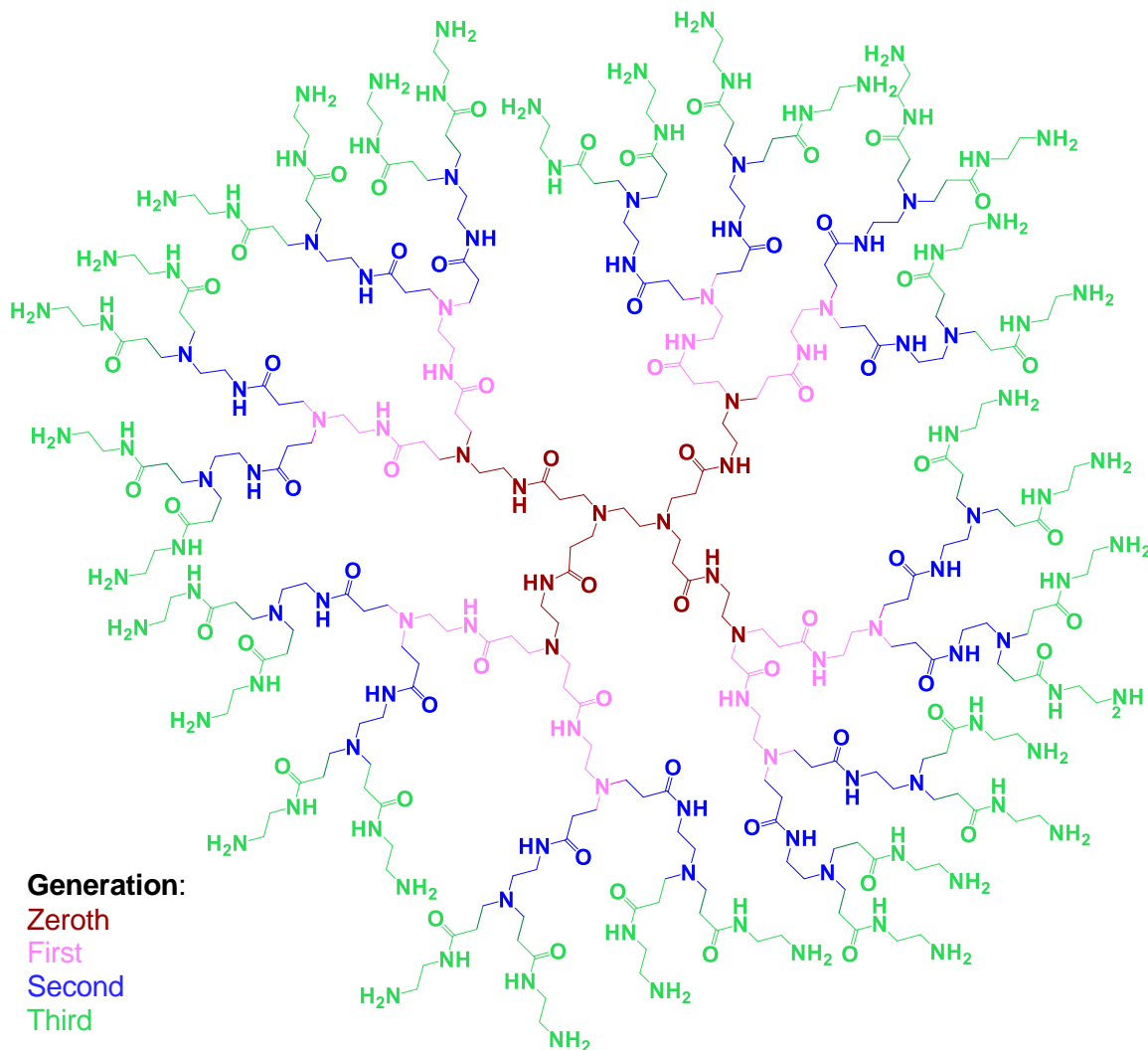


**Figure I.1:** Mixed-matrix polymeric-particle (M2P2) membranes. **A.** Schematic for M2P2 membrane fabrication with in situ synthesis of PEI microgel particles. **B.** Scanning electron micrographs of membrane cross sections. Nonsolvent induced phase separation produces a gradient structure across the depth of the membrane (left) as well as a thin, dense "skin" of PVDF. Condensed microgel particles are dispersed below the skin, anchored in the lace-like PVDF matrix (right).

PVDF: poly(vinylidene fluoride), scaffold polymer. PEI: poly(ethyleneimine), functional polymer/ microgel precursor. ECH: epichlorohydrin, crosslinking agent.

The development of M2P2 membranes stemmed from Diallo's work with Goddard on poly(amidoamine) (PAMAM) dendrimers<sup>26,27</sup> (**Fig. I.2**). Diallo and Goddard reported amine-containing dendrimers as a new class of metal ion chelators, demonstrating the substantial improvement in copper (II) chelation capacity of eighth-generation (G8) PAMAM dendrimer over traditional copper chelating agents<sup>27</sup>. Based on this discovery, Diallo and Goddard invented dendrimer-enhanced ultrafiltration (DEUF), in which an aqueous feed solution is treated with PAMAM dendrimer before passing through an ultrafiltration (UF) membrane<sup>26,28</sup>. The PAMAM selectively bound Cu(II) in the contaminated feed water, and the dendrimer-metal ion complex was rejected by the UF membrane. The retained PAMAM/Cu-

laden solution was then treated with acid to release the Cu(II) ions and regenerate PAMAM. Other dendrimers such as poly(propyleneimine) have been shown to specifically bind perchlorate and uranium (VI)<sup>28</sup>. These target ions are relevant to groundwater purification and resource recovery, respectively.



**Figure I.2:** Third-generation poly(amidoamine) dendrimer (G3-PAMAM). Dendrimers exhibit a "branched-upon-branched" architecture (with degree of polymerization described by the generation), which leads to unusual container-like properties at sufficiently high generations. For PAMAM dendrimers, the container threshold begins at the fourth generation. Note: Terminal groups of dendrimers are distributed throughout the pervaded volume in solution<sup>29</sup>.

While amine-containing dendrimers offer promising chelating abilities for water purification, their synthesis is time- and cost-prohibitive for large-scale production<sup>30</sup>. Furthermore, DEUF suffered from fouling by the dendrimer on the surface of the UF membrane, reducing both flux of water and recovery of dendrimer over time<sup>26</sup>. Therefore, Diallo and Goddard turned to a less expensive substitute for the highly ordered, monodisperse dendrimers: hyperbranched polyethyleneimine (PEI). Crosslinking PEI with acid chlorides, epoxides, and alkyl halides yielded polymer networks that could be applied to nanofiltration and ion-selective resins<sup>31,32</sup>. The net charge of PEI can be tuned by the pH of the solution, enabling ion rejection, ion chelation, or a platform for further functionalization. Diallo and Goddard demonstrated these properties thoroughly with high molecular weight, branched PEI (~10,000 g/mol), and synthesized ion-selective resin beads on the order of hundreds of microns in diameter.

With a demonstrated potential for functionalizing branched PEI, Diallo sought to apply this platform to mixed-matrix UF membranes. The typical preparation of mixed-matrix membranes involves dispersion of externally synthesized particles into a polymer solution followed by casting a film from the dispersion. This preparation strategy was well established for metallic nanoparticles and zeolites, but when the target particle is an organic polymer microgel, particle synthesis presents a host of problems. In order to control the size and distribution of the polymeric particle, emulsion or inverse-suspension systems are necessary; such systems are affected by many parameters and require tedious purifications. Additionally, polymers with different functions are typically immiscible, stemming from the near-zero entropic gain of mixing that is paired with an often-positive enthalpy of mixing for polymers with complementary functions.

Avoiding the unfavorable thermodynamics of mixing polymers, the Diallo Group combined a scaffold polymer in solution with a small nitrogen-rich functional precursor, rather than a preformed polymer<sup>21,22</sup>. The precursor is polymerized *in situ* amidst the scaffold polymer which kinetically frustrates the two components, preventing them from undergoing large scale phase separation despite their immiscibility. After the functional precursor has fully grown

into microgel particles, the casting solution is plunged into a nonsolvent, rapidly precipitating the scaffold polymer and cementing the metastable structure formed during *in situ* polymerization, by nonsolvent-induced phase separation (NIPS). The performance of the subsequent M2P2 membrane is dictated by the complex hierarchical structure of the casting solution that is inaccessible by any other synthetic approach.

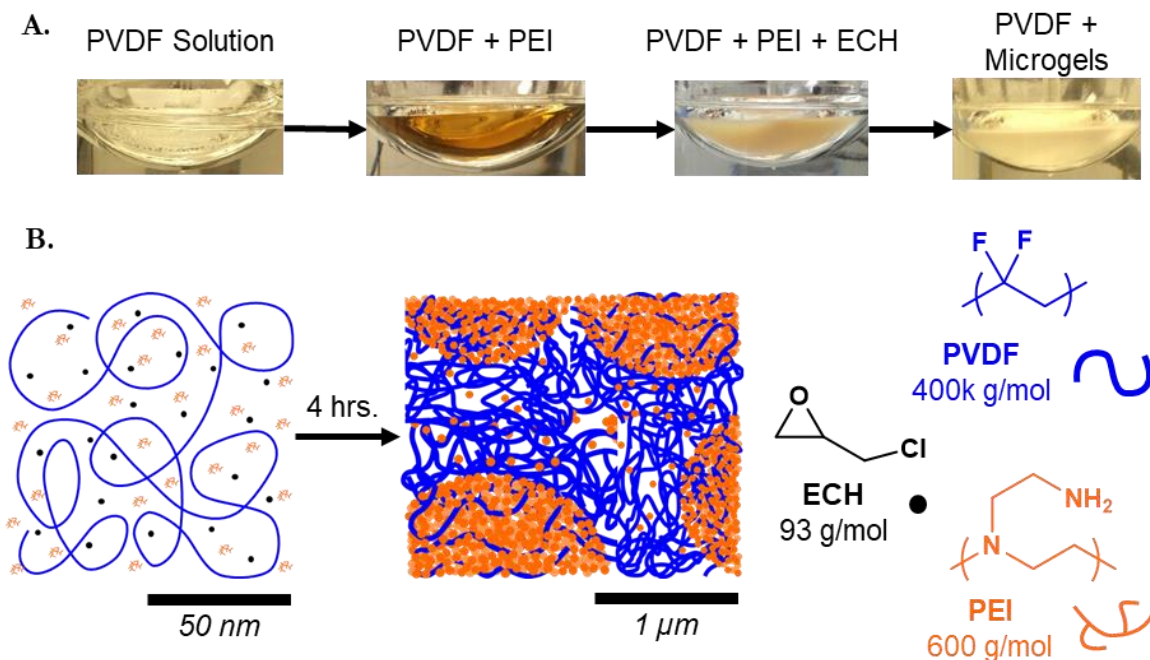
Following the establishment of M2P2 membranes for high-flux water purification, the Diallo Group demonstrated performance for a variety of other applications in proof-of-concept studies. The incorporation of poly(ethylene glycol) (PEG) into PEI microgels afforded exceptional resistance to biofouling<sup>22</sup>, particularly beneficial for microalgae recovery and other biological separations. Using low-generation (*i.e.* G0, G1) PAMAM dendrimers as the microgel precursors, Diallo demonstrated that the container-like properties of higher-generation PAMAMs could be replicated in M2P2 membranes, forming what he termed “dendrimer-like particles.” Membranes with PAMAM-based microgels were applied to metal ion chelation in two applications: copper sorption<sup>24</sup> and catalysis<sup>25</sup>. In the latter, platinum ions were loaded into a PAMAM-based M2P2 membrane and reduced to form Pt nanoparticles encapsulated within the dendrimer-like particles. The catalytic material was then used to reduce acetylene, applying the concept of dendrimer-encapsulated catalytic nanoparticles pioneered by Crooks<sup>33–35</sup>. While these applications have been demonstrated in a proof-of-concept capacity, optimization and implementation in industrial processes requires understanding the process-structure-function relationship and the mechanisms of structure formation during *in situ* synthesis.

## I.2 *In situ* Synthesis: The Solution and the Challenge

In M2P2 membranes, the mechanical robustness of a scaffold polymer is complemented by the tunable functionality of nitrogen-rich polymers through *in situ* synthesis of microgels. While this approach overcomes a significant challenge in the preparation of multicomponent polymer membranes, this also introduces the complex kinetics of polymerization induced phase separation (PIPS); as the functional microgel is grown *in situ*, the increasing molecular weight becomes a driving force for microphase separation—which in turn affects the kinetics of later-stage polymerization. Understanding these competing kinetics and phase transitions is crucial to controlling microstructure and performance in M2P2 membranes. To elucidate the kinetics that govern structure formation in the casting solution, we used a model M2P2 system, selected from Diallo's work<sup>21</sup>.

We use polyvinylidene fluoride (PVDF;  $M_w \sim 400$  kg/mol) as our model scaffold polymer due to its mechanical robustness and chemical resistance to many environments; these features make PVDF a common choice in industrial UF of water. As the precursors to functional particles, we use oligomeric hyperbranched PEI ( $M_w \sim 0.6$  kg/mol) and crosslinking agent epichlorohydrin (ECH;  $M_w \sim 0.1$  kg/mol). The combination of primary, secondary, and tertiary amines of PEI make it ideal for various applications including fouling resistance, post-fabrication functionalization, and metal chelation, while the dense branching ensures the formation of microgel particles.

After PEI is added to a concentrated solution of PVDF (11% by weight), an amber color develops, while the two individual polymer solutions are colorless (**Fig. I.3A**). The casting solution becomes turbid upon addition of catalytic hydrochloric acid and ECH, and a dramatic increase in opacity and viscosity is observed following microgel synthesis. As the *in situ* crosslinking proceeds, the build-up of molecular weight of the PEI drives composition fluctuations to higher and higher amplitudes, by a process called polymerization induce phase separation (PIPS) (**Fig. I.3B**). The entire crosslinking reaction is completed within four hours at elevated temperature.



**Figure I.3:** Depiction of phase behavior during M2P2 membrane synthesis. **A.** Pictures taken at specific points during synthesis, showing visible changes in the casting solution. **B.** Cartoon representation of composition fluctuations at the beginning (left) and end (right) of the crosslinking reaction, shown for different lengthscales. In the left panel, the orange PEI chains and blue PVDF chain are drawn to scale based on molecular weight. Prior to crosslinking, PEI oligomers behave like small molecules with respect to PVDF. PEI: poly(ethyleneimine). PVDF: poly(vinylidene fluoride). ECH: epichlorohydrin.

### I.3 Objectives

Prior to this work, research on this new platform for multicomponent polymer membranes has focused on application. However, performance of M2P2 membranes is intimately tied to the complex hierarchical structure that forms during *in situ* synthesis, as sub-nanometer molecular interactions propagate to micrometer-scale phase transitions. Understanding structure formation and the interplay of different components is therefore paramount to realizing the full potential of these multifunctional materials. A physical description does not yet exist for the competing kinetics of new polymer formation, microphase separation, and subsequent kinetic trapping by phase inversion. Herein I have sought to develop such a description, thereby expanding upon the chemical tools for integrating diverse polymers into multifunctional membrane materials.

*Chapter II***PROBING STRUCTURE FORMATION IN M2P2 MEMBRANES USING NEUTRON SCATTERING**

*Scattering data collection in this chapter, including development of the transient USANS technique, was in collaboration with Joey Kim, Ph.D. R.R.F. designed the study, secured beamtime, optimized reaction conditions, prepared samples, and acquired & analyzed data.*

**II.1 Introduction**

With mixed-matrix polymeric particle (M2P2) membranes, we combine the mechanical robustness of fluoropolymers with the expansive and tunable functionality of branched nitrogen-rich polymers, with demonstrated applications in electrochemical catalysis<sup>25</sup>, fouling-resistant water purification<sup>21,22</sup>, and resource recovery<sup>23,24</sup>. Characterization methods employed thus far have been conducted only on the final M2P2 membrane—and often under vacuum conditions. Yet, as the membrane dries, the shape of the particles and the position of the scaffold polymer are inevitably altered. Moreover, because solidification by nonsolvent-induced phase separation (NIPS) effectively traps the transient nano- and microstructure of the casting solution, controlling membrane performance rests in understanding structure evolution in the casting solution.

The lengthscales of hierarchical structure in casting solutions present a challenge: how can we “see” the different constituents during microgel synthesis? The system is too opaque to measure transient structure with light scattering (**Fig. I.3A**), and the components lack sufficient x-ray contrast. As a nondestructive bulk probe of nano- and microstructure with sensitivity to deuterium labelling, neutron scattering would be ideal. However, neutrons have

limited ability to track transient structure, particularly in the microscale regime crucial to *in situ* microgel synthesis.

While select studies of nanostructured systems have utilized transient small-angle neutron scattering (SANS<sup>36</sup>; 1 – 100 nm), analogous methods for microstructure using ultra-small-angle neutron scattering (USANS; 100 nm – 20  $\mu\text{m}$ ) are lacking. In USANS instruments, the high angular resolution corresponding to microscale structure is achieved using an analyzer crystal that selects a very narrow solid angle, which is rotated to acquire a scattering pattern one angle at a time (**Fig. A.1**, Appendix A)<sup>37–40</sup>. Taken alongside the relatively low incident flux and scattering cross sections inherent to neutron scattering, the resulting USANS guidelines recommend several hours of acquisition per scattering pattern. Breaking from the conventional wisdom, we developed a broadly applicable approach to the characterization of evolving microstructure with USANS.

## II.2 Methods

### II.2.1 Standard synthesis of M2P2 membranes

A typical M2P2 membrane is prepared as follows. A 250 mL three-neck round-bottomed flask is charged with 3.3 g poly(vinylidene fluoride) (PVDF; Kynar 761, 400 kg/mol; gift from Arkema) and 18.5 mL of triethylphosphate (TEP; Sigma Aldrich). The flask is fitted with a mechanical stirrer through the central neck with an appropriate greased adapter and placed in an oil bath set to 80°C. The other two necks are closed with rubber septa, and the mechanical stirrer is set to 40 RPM for the first ten minutes, then increased to 200 RPM overnight. A solution of 2.25 g of poly(ethyleneimine) (PEI; 600 g/mol, Polysciences) and 3 mL of TEP is prepared in a 20 mL scintillation vial. As a viscous liquid, PEI is weighed directly into the scintillation vial using a spatula. The vial of PEI and TEP is sealed, shaken vigorously for 60 seconds, then left to equilibrate at room temperature overnight.

After both the PVDF solution and the PEI solution have homogenized, the round-bottomed flask is flushed with N<sub>2</sub> for approximately 20 minutes, with outlet from a needle in



one of the septa. The PEI solution is transferred slowly to the round-bottomed flask via Pasteur pipette, with N<sub>2</sub> continuing to flow through. The septum is replaced, N<sub>2</sub> flux is reduced accordingly, and the two polymers are allowed to mix for 10 minutes. During this time, a deep amber color emerges, whereas the two individual polymer solutions were colorless (**Fig. I.3A**). The solution remains transparent, indicating no phase separation has occurred. Next, 0.1 mL of 12 M HCl (Sigma Aldrich) is added to the flask dropwise, upon which the mixture immediately becomes clouded. After an additional 15 minutes given for HCl to be dispersed, 1.22 mL of epichlorohydrin (ECH; Sigma Aldrich) is added dropwise to the reaction flask via syringe. The flask is then sealed, N<sub>2</sub> flux is discontinued, and the mixture is allowed to react for four hours. Throughout this process and subsequent reaction, heating is maintained at 80°C and the mechanical stirrer operates at 200 RPM.

After the four hours of reaction, the mixture becomes a viscous dispersion similar in color and consistency to pancake batter (**Fig. I.3A**). Stirring is halted and vacuum is pulled on the flask for about 5 minutes at elevated temperature to remove large bubbles. The stirrer is then removed and approximately half of the casting solution is poured onto a poly(ethylene terephthalate) (PET) nonwoven support taped to a glass plate. The solution is spread into a uniform film with a casting knife set to 300 μm in depth (BYK-Gardner model 2328). After allowing 60 seconds for thermally induced phase separation (TIPS), the film is immersed in deionized water to initiate NIPS. Two hours following the initial immersion, the water bath is replaced. The membrane is kept in water for at least 12 hours and up until further use. For purposes of characterization by scanning electron microscopy (SEM), the film is cast directly onto the glass plate, without the PET support.

## II.2.2 Vial-scale experiments

Samples intended for visual observation of the effects of pairwise sets of components in the casting solution were prepared on the 5–10 g scale in scintillation vials. For samples containing only one polymer, either PEI or PVDF was weighed directly into the vial following an appropriate volume of solvent, TEP or N-methylpyrrolidone (NMP; Sigma Aldrich), measured via syringe or micropipette. Vials were heated using a hot plate, either in an oil bath

or heating block. Additional components (ECH or HCl) were added via syringe. For vial-scale samples containing both PEI and PVDF, they were dissolved separately in similar fashion to standard M2P2 membrane preparation; approximately 15% of the total intended solvent was used to dissolve PEI in a separate vial at room temperature while PVDF dissolved in the remainder of solvent at elevated temperature. Ratios of components for a representative sample at the 5 g scale is shown in **Table II.1**. Samples were assessed qualitatively, observing color, viscosity, and turbidity changes by eye.

### II.2.3 Preparation of samples for neutron scattering experiments

Neutron scattering samples were prepared for cylindrical cells with 2 mm path length and 560  $\mu\text{L}$  capacity (Hellma Analytics). To facilitate mixing at different levels of solvent deuteration, we prepared stock solutions containing PVDF and PEI at double their intended compositions (12.2% and 8.4%, respectively), with duplicate stocks in hydrogenous NMP and deuterated NMP- $d_9$  (Cambridge Isotope). The discrepancy in solvent from standard M2P2 membrane synthesis was due to lack of commercial availability of deuterated TEP. To account for the much lower concentrations of ECH paired with small sample size, a 20% (v/v) stock solution of ECH in NMP- $d_9$  was prepared rather than adding neat ECH to the sample; we considered the volume of solvent added via the stock ECH solution to be negligible to the overall concentrations ( $\sim 20 \mu\text{L}$ ). Similarly, a 5% (v/v) stock solution of 12 M HCl in NMP- $d_9$  was prepared.

As an example, preparation of a sample with intended composition 6.1% PVDF, 4.2% PEI, and 0.4% ECH by weight in 80% deuterated NMP proceeded as follows. In a half-dram vial, 240  $\mu\text{L}$  each of PVDF stock in NMP- $d_9$  and PEI stock in NMP- $d_9$  were combined with 60  $\mu\text{L}$  each of PVDF and PEI stocks in hydrogenous NMP. Solutions were mixed with a syringe equipped with a blunt Teflon needle and loaded into a banjo cell. Immediately prior to placing samples in the beam, 9.35  $\mu\text{L}$  of ECH stock and 18  $\mu\text{L}$  of HCl stock were added to the cell (without mixing). The composition of USANS casting solutions compared to standard M2P2 membrane synthesis is shown in **Table II.1**.

**Table II.1:** Representative sample compositions for different types of experiments

Component	Standard M2P2		USANS samples		Vial-scale	
	Amt. (g)	wt. %	Amt. (g)	wt. %	Amt. (g)	wt. %
<b>PVDF</b>	3.30	11	0.034	6.1	0.305	6.1
<b>PEI</b>	2.25	7.5	0.024	4.2	0.21	4.2
<b>ECH</b>	1.44	4.8	0.002	0.4	0.04	0.8
<b>HCl (12 M)</b>	0.12	<0.2	0.001	<0.2	0.005	<0.2
<b>TEP</b>	23.0	76.7	-	-	-	-
<b>NMP</b>	-	-	0.500	89.3	4.445	88.9

## II.2.4 Small angle neutron scattering experiments

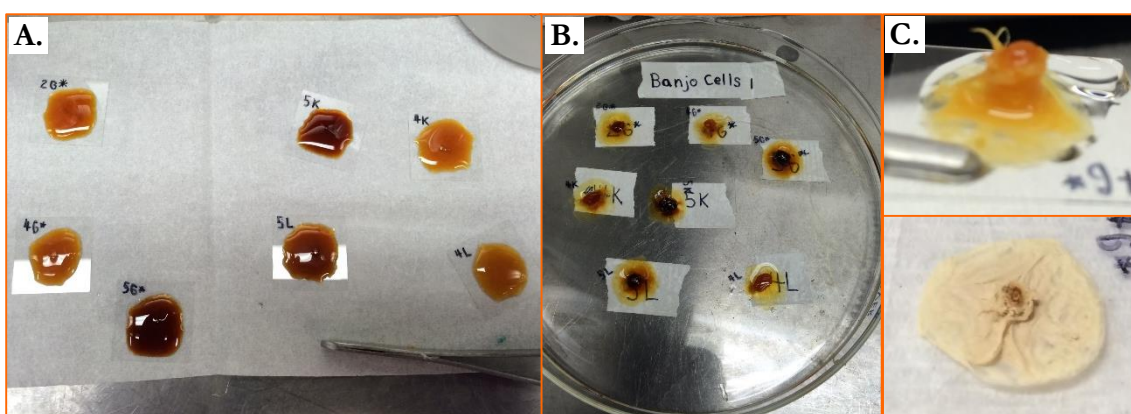
SANS measurements were conducted at the NIST Center for Neutron Research (NCNR) using the NGB and NG7 30m SANS instruments. Both instruments cover lengthscales from ~1 to 500 nm; achieve wavelength resolution of 10% – 30% (FWHM); and utilize a 640 mm x 640 mm  $^3\text{He}$  position-sensitive proportional counter with 5.08 mm x 5.08 mm pixels. Continuously variable sample-to-detector distances (SDDs) for NG7 are in the range of 1.0 to 15.3 m, while SDDs for NGB span 1.3 to 13.1 m. A 6-sample banjo cell changer with controllable temperature was used in both cases. Most SANS data was acquired on NGB in February 2016, while select follow-up measurements on NG7 were collected the following month, March 2016. Unless otherwise indicated, SANS data were acquired on NGB.

## II.2.5 Ultra-small angle neutron scattering experiments

USANS measurements were conducted on the BT5 Perfect Crystal Diffractometer at the NCNR, with incident beam wavelength of 2.38 Å and 6%  $\Delta\lambda/\lambda$  (FWHM) and ~17,000 neutrons/cm<sup>2</sup>s current at sample. The monochromator and analyzer are triple-bounce Si(220) crystals. Transient USANS experiments were conducted in two beamtime allocations, one in February 2016 and one in February 2019. The analyzer accepts a solid angle of  $7.1 \times 10^{-7}$  sr and has a slit height of  $0.117 \text{ \AA}^{-1}$  in reciprocal space.

## II.2.6 Drop casting of films from USANS samples

Following USANS experiments, some samples were solidified for further analysis by SEM. Due to the small volume of each sample (560  $\mu\text{L}$ ), liquid samples were dropped onto a microscope cover slip, via syringe or Pasteur pipet, and spread around. Cover slips were then placed in a petri dish and the dish was filled with deionized water (**Fig. II.1**). Films were kept in water under refrigeration for several hours then transferred to small plastic sealable bags for transport.



**Figure II.1:** Drop-cast films from USANS samples, prior to (A) and after (B) immersion in water. C. Wet film after removal from water (top) and dry film after storage in air for several months (bottom).

## II.2.7 Scanning electron microscopy

SEM samples were prepared from solid films in the following manner. Films were dried in a vacuum oven overnight to remove all water. Small pieces were cut  $\sim 1 \text{ cm}^2$  with scissors to characterize the membrane surface; the top surface of unsupported membranes were typically matte while the bottom surface was glossy. Cross sectional samples were prepared by immersing the dried film in liquid  $\text{N}_2$  for a  $\sim 10$  seconds then fracturing the membrane.

Samples were mounted on SEM stubs using carbon tape and sputter-coated with a 10 nm layer of platinum. Micrographs were obtained using a Zeiss 1550VP Field Emission SEM,

using either in-lens or below-lens scanning electron detectors and an electron high tension voltage of 5 – 10 kV, depending on the sample.

## II.2.8 Plotting color scheme

In plots containing the blue-brown color scheme, colors were drawn from Peter Kovesi's colorblind-distinguishable version of the Viridis colormap, named CET\_CBTL2<sup>41</sup>. Colors are scaled to reaction time within a single plot.

## II.3 Results & Discussion

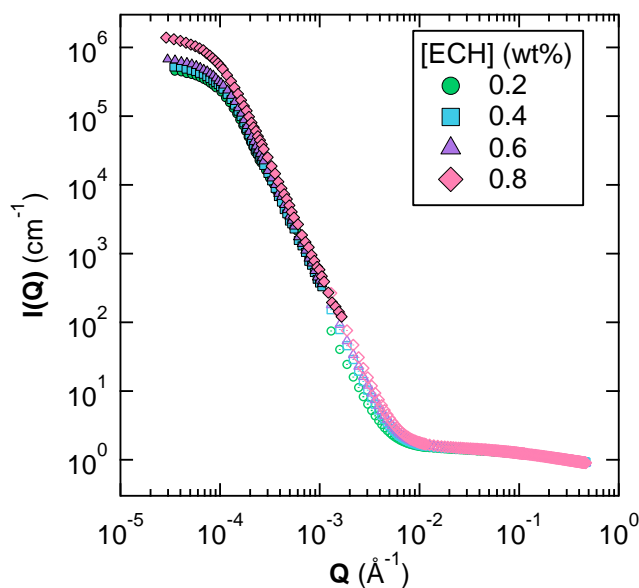
### II.3.1 Equilibrated structure in final casting solutions

We began by measuring structure in equilibrated casting solutions for a range of crosslinker concentrations using both SANS and USANS (**Fig. II.2**). In this set of samples, we used reduced concentrations of ECH as a proxy for different extents of reaction, in the hopes of gaining insight into the mechanism of structure formation with respect to ECH content.

As explained in Appendix A, USANS data are slit-smear<sup>42</sup> due to the geometry of the instrument. While an algorithm was developed by Lake<sup>43</sup> for numerically removing the effects of slit-smearing from USANS data point-by-point, the method can be prone to introducing artefacts in the "de-smear<sup>43</sup>" data. Therefore, we chose not to de-smear USANS data, instead bearing in mind that power law exponents in fitted USANS data were approximately one larger than the true sample scattering (*e.g.* a  $Q^4$  feature is smeared in USANS to appear like  $Q^3$ , Fig. II.2). In global scattering plots, we applied the slit-smearing convolution to SANS data fitted to a sum of two power laws so they may be directly compared to the inherently smeared USANS scattering patterns (Eqn. 12, Appendix A). The pinhole geometry of SANS causes negligible smearing<sup>43</sup>.

**Table II.2:** Fit parameters for constituent power laws of SANS data. The sum of the two power laws were slit-smearred and renormalized.

[ECH] (wt%)	SANS low-Q		SANS high-Q	
	$A_1$	$m_1$	$A_2$	$m_2$
0.2	$2.74 \times 10^{-9}$	4.2	0.29	0.20
0.4	$1.76 \times 10^{-9}$	4.4	0.29	0.21
0.6	$2.35 \times 10^{-9}$	4.3	0.28	0.22
0.8	$1.61 \times 10^{-9}$	4.5	0.28	0.24



**Figure II.2:** Global scattering from fully reacted casting solutions. SANS data (open markers) have been fit to a sum of two power laws and the smooth function was computationally slit-smearred (see Appendix A.3.3). Closed markers: USANS.

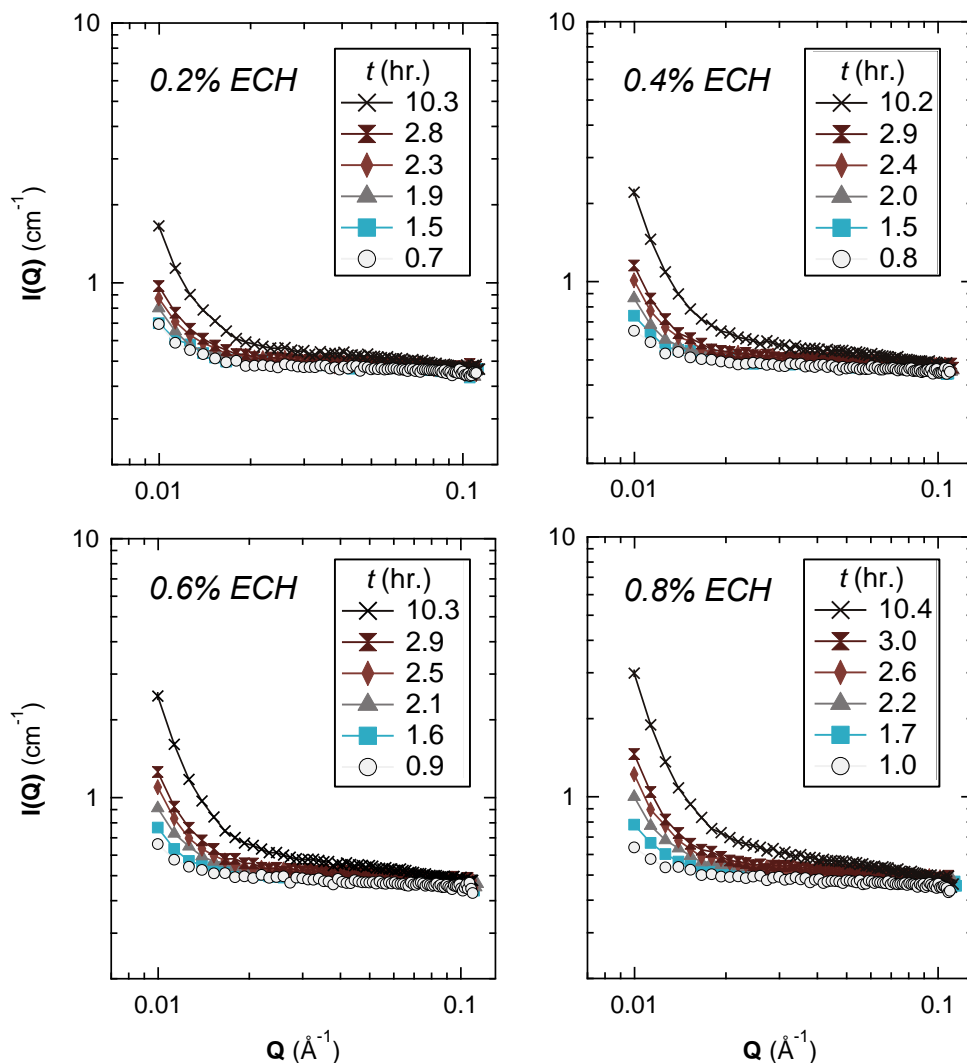
Composition: 6.1% PVDF, 4.2% PEI, 0.01% HCl in 80D:20H-NMP.

Global scattering patterns of casting solutions which had reacted for over a day were remarkably similar across different concentrations of ECH (**Fig. II.2**). This suggests that [ECH] does not appreciably impact the final structure in casting solutions. We found these results promising: The final structure being insensitive to [ECH] suggests that we can vary [ECH] to slow down the crosslinking reaction and might still obtain information relevant to

the actual M2P2 membrane synthesis. Therefore, we turned to time-resolved SANS, an established method for slow kinetics experiments with neutron scattering (acquisition times  $\sim 5$  min.).

### **II.3.2 Time-resolved SANS of M2P2 casting solutions**

Time-resolved SANS on casting solutions of the same composition as the final state scattering patterns shown in Fig. II.2 revealed that the bulk of structure formation during *in situ* polymerization occurs at the microscale rather than nanoscale (**Fig. II.3**). Intramolecular structure changes little after the first few minutes of reaction; thus, to learn the kinetics of microgel synthesis, we must find a way to observe time-dependent structure in the microscale regime probed by USANS.



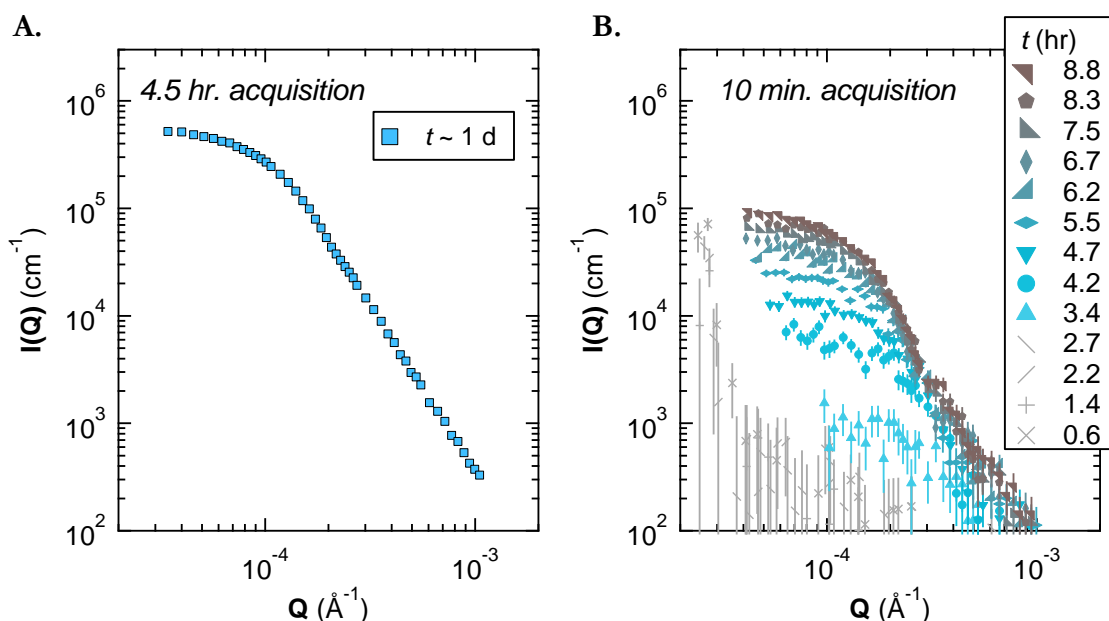
**Figure II.3:** Time-resolved SANS of casting solutions. Very little changes are observed in the lengthscales probed by SANS, corresponding to intramolecular polymeric structure.

### II.3.3 Time-resolved USANS

Conventional USANS guidelines recommend acquisition times on the order of several hours. With the entire microgel crosslinking reaction occurring within just four hours, we faced two questions regarding the feasibility of observing structure formation: (i) What is the minimum acquisition time for USANS? and (ii) Can we create a “slow-motion” version of our model system? In service of the first question, examination of USANS data obtained using the



conventional acquisition time (4.5 hours) on fully reacted casting solutions revealed high signal-to-noise (**Fig. II.2**, closed markers). We posited that we could reduce the acquisition time appreciably while preserving the general features of the pattern. In M2P2 membrane casting solutions, polymerization of PEI into crosslinked microgels is in kinetic competition microphase separation induced by that polymerization. To create a slow-motion version of this system (addressing the second question), we must reduce the rate of both of these processes to similar extents. We did this by reducing the relative concentration of crosslinker with respect to PEI oligomer, and diluting all the constituents. Taken together, we found that we could measure transient structural development in our slowed-down model using just ten minutes of acquisition—an order of magnitude improvement upon conventional USANS (**Fig. II.4**).



**Figure II.4:** Conventional (**A**) and time-resolved (**B**) USANS patterns for casting solutions with the same composition and contrast: 6.1% PVDF; 4.2% PEI; 0.4% ECH; 0.1% HCl. The solvent is a mixture of 80% NMP- $d_9$  and 20% hydrogenous NMP. All percentages are w/w. Note: error bars are shown for all data; if not visible, they are smaller than the size of the markers.

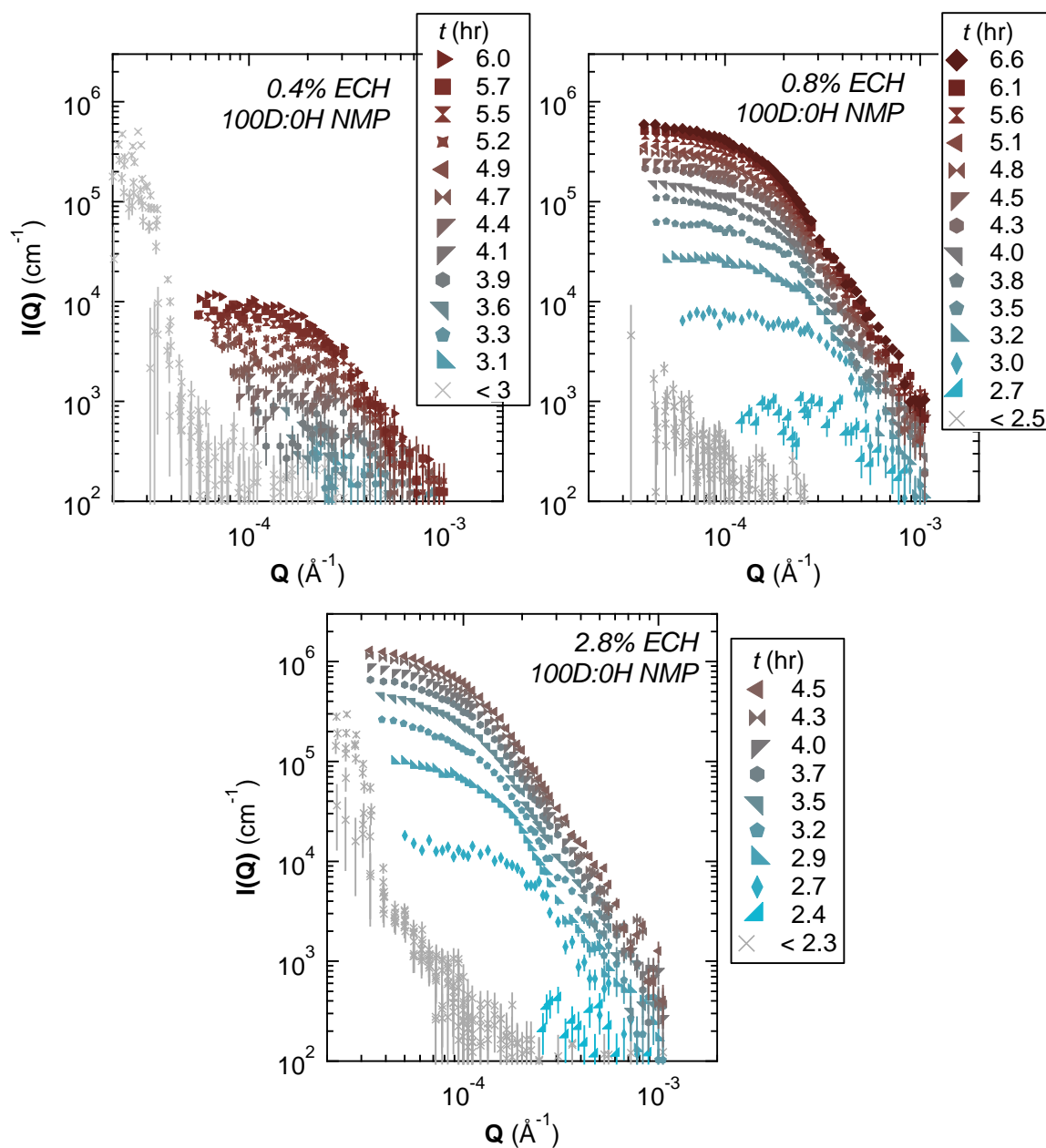
The substantially shorter acquisition times required us to deviate from NCNR's standard data reduction protocol<sup>44</sup>, particularly regarding the subtraction of the empty cell scattering, a.k.a. the “Q-dependent background.” Rather than using the single 4.5-hour measurement on the empty cell, with splines between data points (NCNR's standard protocol), we fit a set of five measurements that could be considered blanks to a smooth piecewise function for the Q-dependent background,  $I_{\text{QDB}}(\text{Q})$ . Additionally, we quantitatively defined the “Q-limit of detection” ( $Q_{\text{LOD}}$ , the lowest Q value for which sample scattering could be reliably distinguished from the background), specific to each reaction time based on the ratio of sample scattering to background scattering. For a full discussion of the unique challenges of reducing and correcting USANS data compared to typical scattering experiments, including how we determined  $I_{\text{QDB}}(\text{Q})$  and  $Q_{\text{LOD}}$ , see Appendix A.

Having reduced acquisition times to ten minutes, we probed the early stages of polymerization-induced phase separation (PIPS)—the first six hours—for several concentrations of ECH (**Fig. II.5**). The highest ECH concentration gives the ratio of ECH:PEI (2:3 by weight) that is used in M2P2 membrane synthesis (at lower overall concentration, Table II.1). In the early stages of reaction, scattering is weak as structure is first being born; therefore, we used pure NMP-*d*<sub>9</sub> as the solvent to increase the scattering contrast. Here and in subsequent time-resolved scattering patterns, all time traces which cannot be distinguished from background are collectively shown as gray Xs (**Fig. II.5**).

### II.3.4 Effects of solvent deuteration and multiple scattering

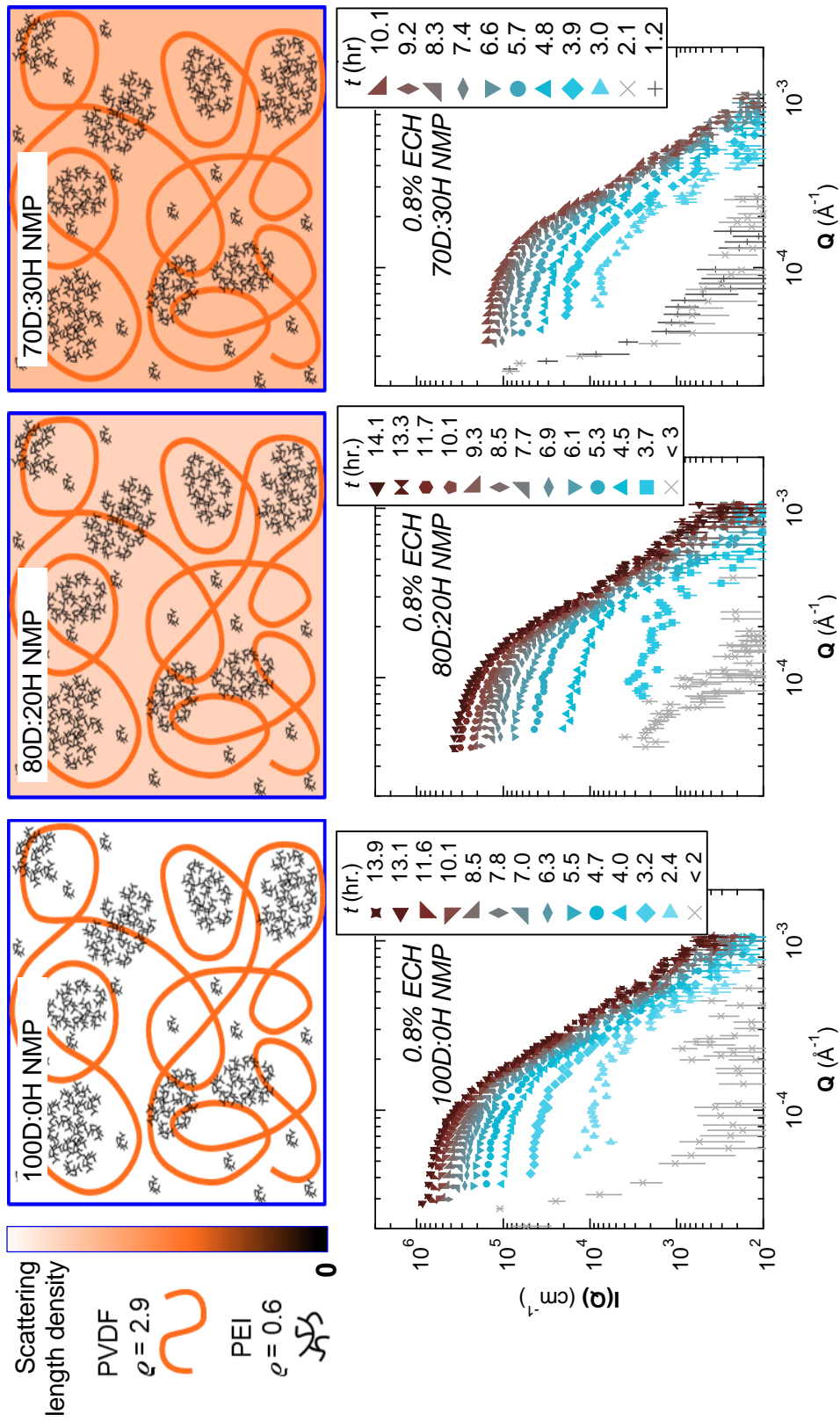
In the present polymerization-induced phase separation process, decreasing the deuteration content of the solvent primarily reduces the contrast in scattering length density and increases incoherent scattering. Both of these effects tend to reduce the magnitude of the coherent scattering pattern. In addition, the change in solvent composition changes the contrast in scattering length density differently for different species (upper half of **Fig. II.6**).

Specifically, when going from 80D:20H NMP to 100% deuterated, the "kink" between the low-Q shoulder and the high-Q power law, around  $Q=3 \times 10^{-4} \text{ \AA}^{-1}$ , was less pronounced. We attribute the masking of this feature to multiple scattering<sup>45</sup>. For reaction times up to 6 hours, scattering from samples in 100% deuterated NMP remained within the NCNR-defined threshold where multiple scattering is negligible<sup>44</sup>. However, scattering patterns for long reaction times in 100% deuterated NMP consistently surpassed the threshold where multiple scattering is non-negligible. Therefore, for longer reaction times, we focused our kinetic analysis on samples in 80D:20H NMP. The lowest level of deuteration we examined was 70%; upon evaluation of scattering patterns we concluded that further reduction of deuteration would have led to intolerably low signal-to-noise for time-resolved experiments, due to incoherent scattering from the total hydrogens. A pictorial representation of the effects of deuterium content in the solvent and analogous time-resolved scattering profiles, are shown in **Fig. II.6**. Scattering profiles across long reaction times with different concentrations of ECH are shown in **Fig. II.7**.

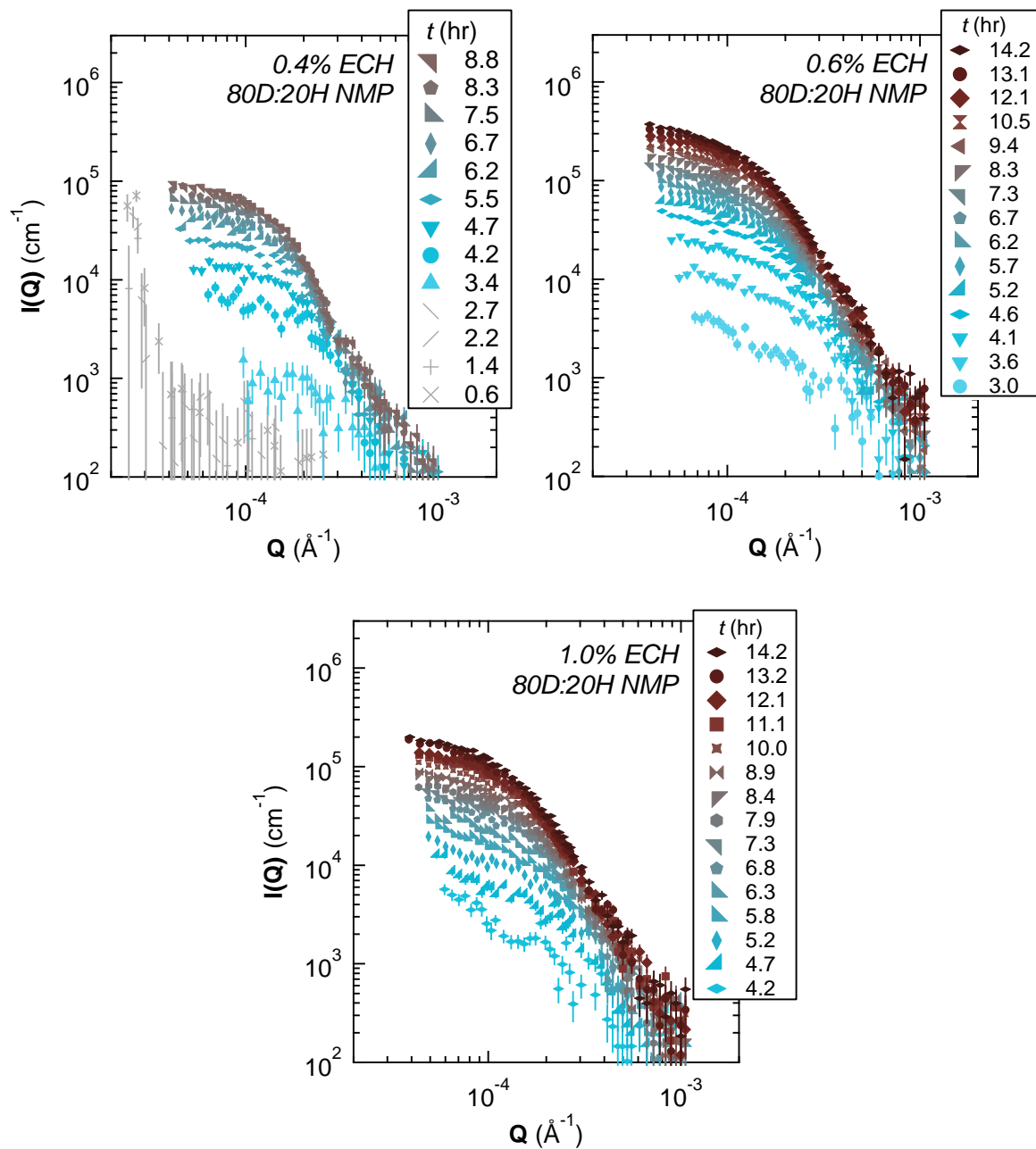


**Figure II.5:** Early stages of phase separation probed by time-resolved USANS. The concentration of crosslinker has a profound effect on early structure development, as expected. Composition: 6.1 wt.% PVDF, 4.2 wt.% PEI, 0.01 wt.% HCl in 100D:0H-NMP.

Note that the 0.8% ECH case is used for the comparison of 100D/0H, 80D/20H, and 70D/30H NMP in the following figure.



**Figure II.6:** Effects of contrast in M2P2 solutions. As the level of deuteration in the solvent, NMP, is decreased (left to right), the contrast of the two polymeric species decrease at different rates, due to their scattering length densities,  $\rho$  ( $\times 10^{-6} \text{ \AA}^{-2}$ ).

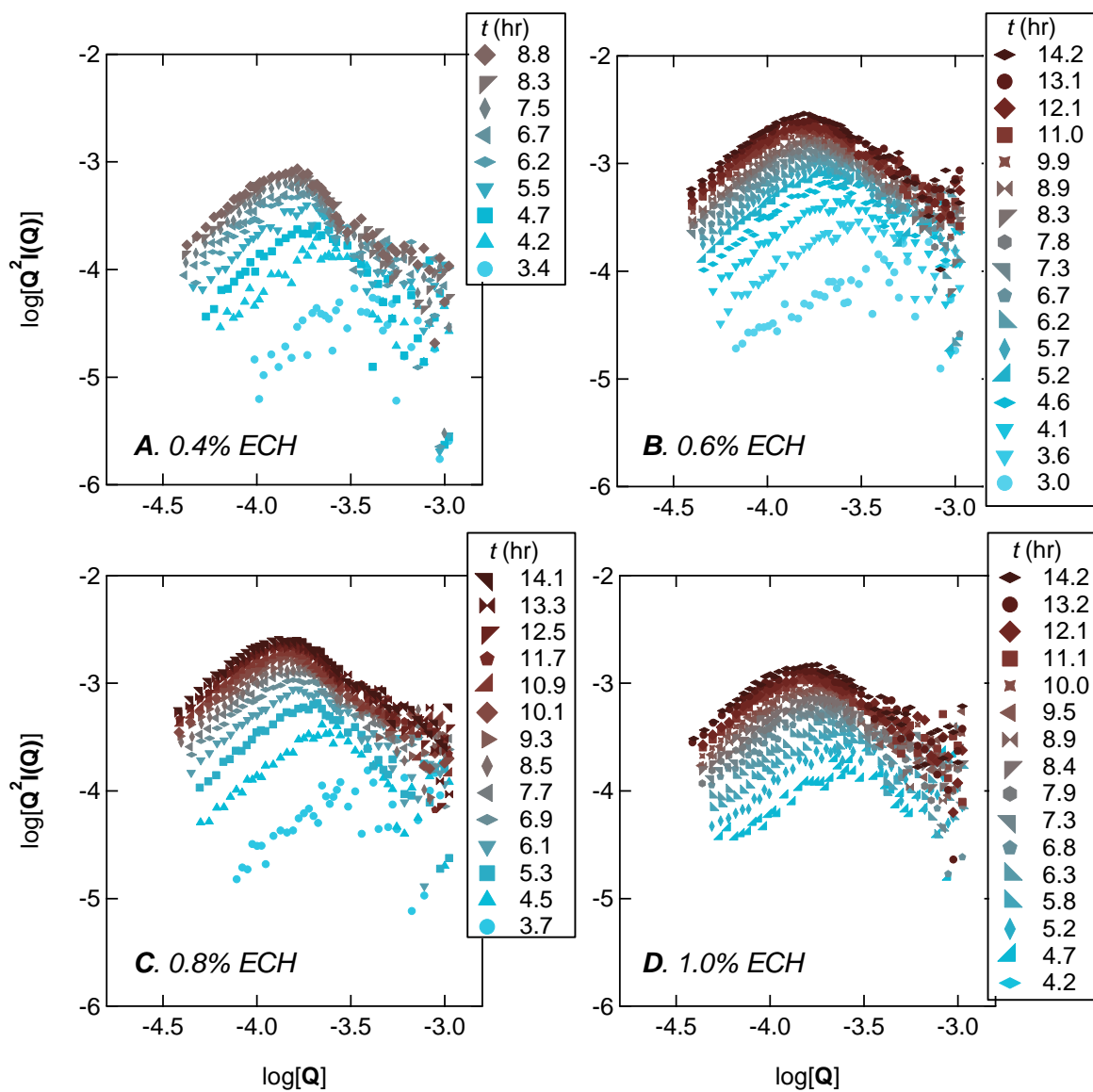


**Figure II.7:** Later stages of phase separation in M2P2 casting solutions, for a range of [ECH].

### II.3.5 Kinetics of structure formation revealed by USANS

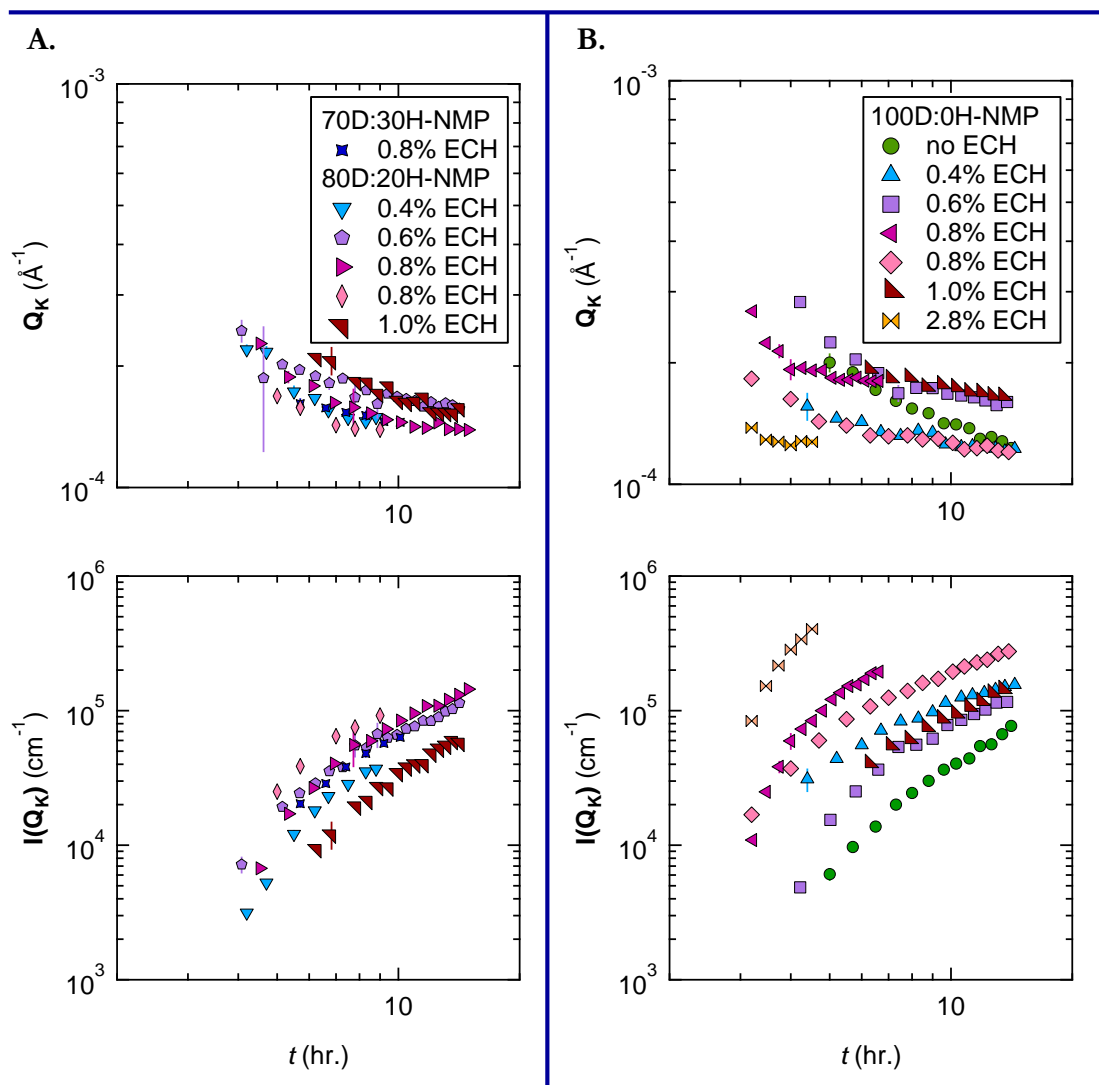
Irrespective of composition, M2P2 casting solutions exhibit an early latent stage in which structure in the USANS Q-range has not yet developed; this latent stage can last several hours (**Fig. II.5 – II.7**). Then, over a single time step, substantial scattering is observed; the time of this onset of USANS signal varies with both [ECH] (**Fig. II.7**) and deuterium content in the solvent (**Fig. II.6**). Likewise, the magnitude of this jump correlates strongly with [ECH], suggesting that [ECH] influences the quench depth induced by microgel synthesis. Eventually, the “high-Q power law” scattering saturates ( $Q > 3 \times 10^4 \text{ \AA}^{-1}$ ;  $\log[Q] = -3.5$ ) while the “low-Q shoulder” continues to increase. As the process continues to longer times, the center of this low-Q shoulder shifts to smaller Q while the intensity continues to increase. The shoulder is more obviously differentiated from the high-Q power law when the solvent is a mixture of hydrogenous and deuterated NMP (**Fig. II.6**).

The longest structural lengthscale is manifested by the Q-value at which the plateau at low-Q begins to roll-off as Q increases, which is readily identified as a peak in a Kratky plot,  $Q^2I(Q)$  vs. Q (**Fig. II.8**). We determined the peak position, denoted  $Q_K$ , by fitting a neighborhood of points around the raw maximum to a parabola (**Fig. B.1**, Appendix B). A priori, the starting and ending values of Q for the neighborhood of the peak are unknown; therefore, we developed a method to identify the range of starting and ending Q-values that yield a consistent value of  $Q_K$  (see Appendix B). The time dependence of  $Q_K$  and  $I(Q_K)$  for several samples are shown in **Fig. II.9**. While we cannot say for certain that  $Q_K$  and  $I(Q_K)$  bear a power law relationship with reaction time, we use power law fits to draw qualitative conclusions about the mechanism of phase separation in M2P2 casting solutions; resultant exponents are shown in **Tables II.3** and **II.4**.



**Figure II.8:** Kratky plots for different concentrations of ECH. Composition: 6.1% PVDF, 4.2% PEI, 0.01% HCl, in 80D:20H-NMP.





**Figure II.9:**  $Q_K$  decreases while  $I(Q_K)$  increases exponentially with reaction time. For many samples,  $I(Q_K)$  exhibits an approximate power law dependence on reaction time for late times, but no single power law describes the full range of times. We visually determined a transition reaction time,  $t_0$ , between early-stage time dependence and late-stage time dependence for such samples.

**A.**  $Q_K$  (top) and  $I(Q_K)$  (bottom) as a function of reaction time for samples with 70% or 80% deuterated solvent. **B.**  $Q_K$  (top) and  $I(Q_K)$  (bottom) as a function of reaction time for samples in 100% NMP- $d_9$ .

Composition of polymers: 6.1 wt.% PVDF and 4.2 wt.% PEI.

**Table II.3:** Power law exponents for  $Q_K$  and  $I(Q_K)$  with respect to reaction time shown in **Fig. II.9A**. In some samples, time dependence was approximated by two power laws; the time transition between regimes,  $t_0$ , was determined visually.

[ECH] (wt.%)	%D in solvent	$t_0$ (hr.)	$m, I(Q_K) \sim t^m$		$m, Q_K \sim t^m$	
			$t < t_0$	$t > t_0$	$t < t_0$	$t > t_0$
<b>0.4</b>	80	7	4.5	1.8	-0.8	$\sim 0$
<b>0.6</b>	80	9	2.2	1.4	-0.3	-0.2
<b>0.8</b>	80	8.5	2.5	1.4	-0.8	-0.1
	70	n/a	2.0	-	-0.2	-
<b>1.0</b>	80	n/a	-	2.1	-	-0.4

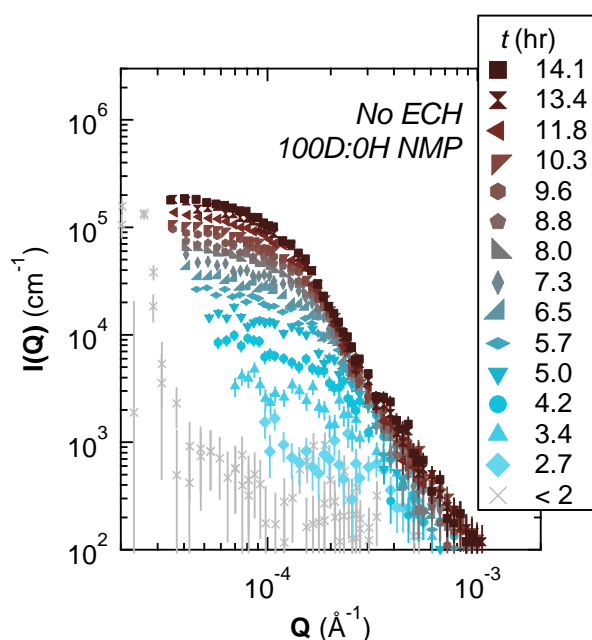
**Table II.4:** Power law exponents for  $Q_K$  and  $I(Q_K)$  with respect to reaction time shown in **Fig. II.9B**.

[ECH] (wt.%)	%D in solvent	$t_0$ (hr.)	$m, I(Q_K) \sim t^m$		$m, Q_K \sim t^m$	
			$t < t_0$	$t > t_0$	$t < t_0$	$t > t_0$
<b>0</b>	100	5	3.0	1.9	-0.6	-0.4
<b>0.4</b>	100	7	1.9	1.0	-0.3	$\sim 0$
<b>0.6</b>	100	4.5	4.5	1.4	-0.8	-0.2
<b>0.8</b>	100	3.5	2.9	1.2	-0.5	-0.2
<b>1.0</b>	100	n/a	-	1.5	-	-0.2
<b>2.8</b>	100	n/a	3.8	-	-0.5	-

The initial decrease in  $Q_K$  indicates an increase in the lengthscale of segregation, which is accompanied by an increase in intensity. After this initial phase,  $Q_K$  becomes relatively constant and the further increase in  $I(Q_K)$  indicates that the degree of segregation of PEI and PVDF is intensifying while the lengthscale only weakly increases<sup>46-50</sup>. We took this time-dependence to indicate that the build-up of molecular weight of PEI into microgels plunges the system into an unstable region of the phase diagram, inducing spinodal decomposition (**Fig. II.9**). However, we could not ascertain a correlation between crosslinker concentration and power law exponent in plots of  $Q_K$  and  $I(Q_K)$  vs. time (**Table II.3**).

### II.3.6 The “control” was not a control

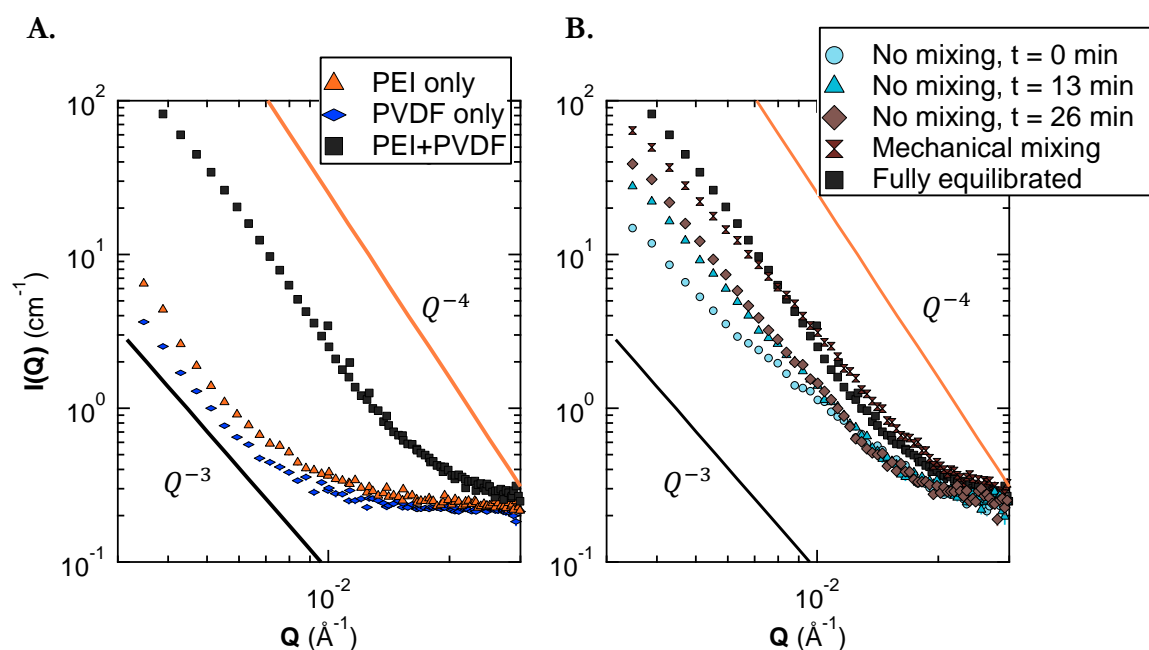
We acquired time-resolved USANS data on M2P2 casting solutions in the absence of crosslinker, intending these samples to be controls wherein microgel synthesis and subsequent phase separation did not proceed (**Fig. II.10**). To our surprise, these ECH-free samples revealed substantial scattering that qualitatively agreed with time-dependent features of casting solutions containing ECH. Therefore, there must be some other chemical or physical interaction in PVDF+PEI solutions in the absence of crosslinker. We probed this structure further with follow-up SANS experiments using NG7.



**Figure II.10:** M2P2 casting solutions without any crosslinker exhibited much of the time-dependent phase behavior observed in samples containing ECH, though we anticipated this to be a control sample

To study the how PVDF interacted with PEI without any external mixing (**Fig. II.11**), we combined stock solutions of 12.2% PVDF and 8.4% PEI in equal volumes and repeatedly acquired SANS patterns at roughly 13-minute intervals. After three acquisitions, the sample was removed and mixed with a syringe until the solution appeared homogeneous (called “Mechanical mixing,” **Fig. II.11B**). For reference, the equilibrated sample first shown in panel

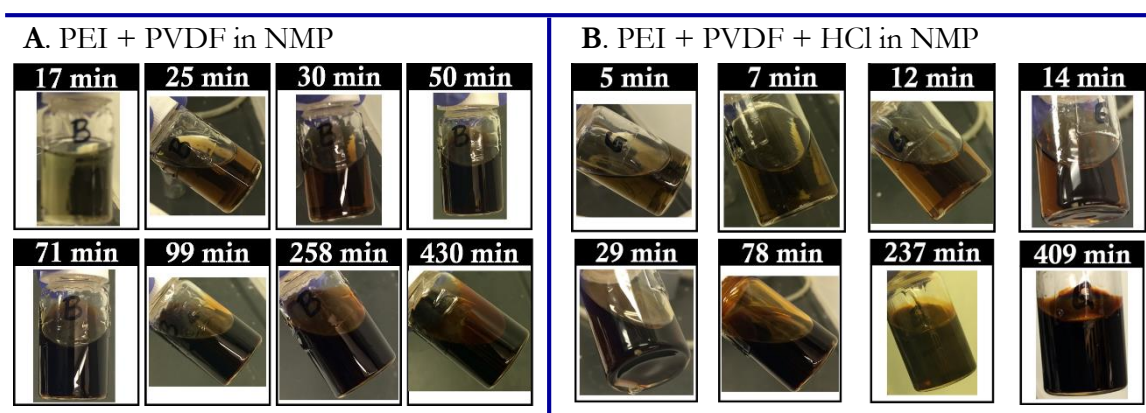
**A** is also included in panel **B**. As degree of mixing increased, the slope generally increased in magnitude, approaching that of the equilibrated sample. In the three traces labelled “No mixing,” the  $Q$ -position of the upturn in intensity remained constant, but mixing resulted in a rightward shift. Overall, the intensity increased with mixing. The Porod exponent approaching  $m = 4$  (orange lines, **Fig. II.12**) indicates the development of intermolecular structures with sharp interfaces<sup>51</sup>.



**Figure II.11:** Interactions of PVDF & PEI. **A.** SANS patterns showing structure develops in mixtures of PVDF and PEI that cannot be explained by simple additive effects of the two constituents. **B.** Upon different degrees of mixing PVDF and PEI, low- $Q$  power law scattering indicates formation of structures with sharp interfaces.

Upon further investigation with vial-scale experiments, we realized that in the absence of crosslinker, PEI and PVDF form a dark brown gel in NMP (**Fig. II.12**), which cannot be reversed by heating or addition of more solvent. A possible chemical explanation for both the color change and structure observed by neutron scattering is that PEI amines dehydrofluorinate the PVDF backbone and become chemically grafted<sup>52–54</sup>. However, because this gelation appears to be accelerated by the presence of HCl (**Fig. II.12B**), an acid-mediated

mechanism is more likely to be the cause. While this process apparently becomes arrested by the addition of the much more reactive ECH in a typical M2P2 membrane synthesis, the brief time between mixing of PEI and PVDF and the addition of ECH could be sufficient for covalent binding of PEI to PVDF. This process could explain why PEI microgels are permanently embedded in M2P2 membranes, whereas other attempts of embedding polymeric particles in mixed matrix membranes fail over time.



**Figure II.12:** In the absence of ECH, PEI and PVDF undergo a chemical gelation process when dissolved in NMP, both without (A) and with (B) catalytic HCl. Color changes first to green, then amber, then deep reddish brown. This process is accelerated when acid is added to the sample.

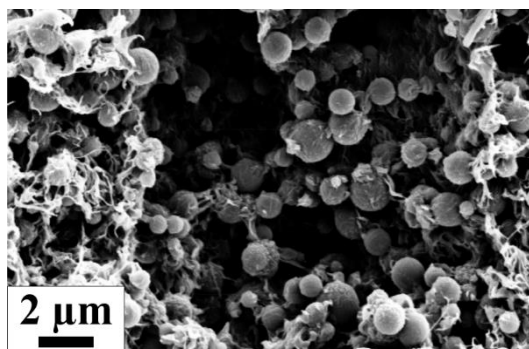
### II.3.7 Comparison to standard membranes by SEM

Following the modified crosslinking reaction measured by transient USANS, the viscous liquid samples were drop-cast onto a microscope cover slip and immersed in water. Several parameters differed between solidified USANS samples and a typical M2P2 membranes (Table II.3). Nonetheless, we sought to compare the solid structures by SEM (Fig. II.11). While we did not see discrete micron-size PEI particles in films from the USANS samples, we did observe small nodules that could be PEI-rich domains covalently bound to PVDF. The significantly decreased amount of ECH included in USANS samples keeps PEI molecular weight below 1500 g/mol, meaning that during NIPS of drop-cast USANS films, most of the PEI likely dissolved into the nonsolvent bath.

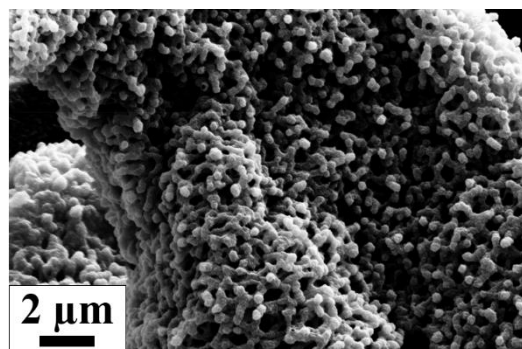
**Table II.5:** Differences in solidification between standard M2P2 membranes and films cast from USANS samples.

Parameter	Standard M2P2	USANS Film
Solvent	TEP	NMP
Total polymer content	23 wt%	11 wt%
Reaction time	4 hrs.	14 hrs.
Casting method	Casting knife	Drop cast

**A.** Standard M2P2 membrane



**B.** USANS sample



**Figure II.13:** Comparing film cross sections for a typical M2P2 membrane (**A**) and a sample modified for time-resolved USANS (**B**). Small nodules in the USANS sample film could be PEI-rich regions which could not coalesce into larger particles due to reduced crosslinker concentration ( $[ECH]=0.4\%$ ).

## II.4 Summary

Since its implementation in the late 1990s, Bonse–Hart USANS has afforded substantial discoveries in systems containing microscale structure<sup>38</sup>, from particle aggregation<sup>55</sup> to polymer blends<sup>56</sup> to porosity of shales<sup>57–59</sup>. In addition to the general advantages of neutrons in being amenable *in situ* experiments and contrast variation by isotopic labeling, USANS offers exquisite angular resolution corresponding to microscale structure—resolving less than  $10^{-5}$  degree<sup>37</sup>. The unusual optics necessary to access such high resolution paired with inherently low flux and scattering propensity of neutrons has led most in the field to presume that kinetic experiments would never be feasible with USANS. Despite this foregone conclusion in the neutron scattering community, we demonstrated an order of magnitude reduction in acquisition time with USANS, enabling the measurement of transient microstructure.

Acquiring each scattering pattern in ten minutes—as opposed to several hours—we conducted a kinetic USANS study on the growth of microgel particles in M2P2 membrane casting solutions. Transient USANS data allowed us to distinguish between multiple competing hypotheses of phase separation during *in situ* synthesis of microgels. The mechanistic insights gained from this study provide an explanation for the pronounced stability and performance of M2P2 membranes. Not only do our results inform membrane design with tunable microstructure, but they also provide a framework for design of future kinetic USANS experiments, germane to the broad class of research problems that involve physicochemical interactions coupled to microstructure evolution<sup>60–63</sup>.

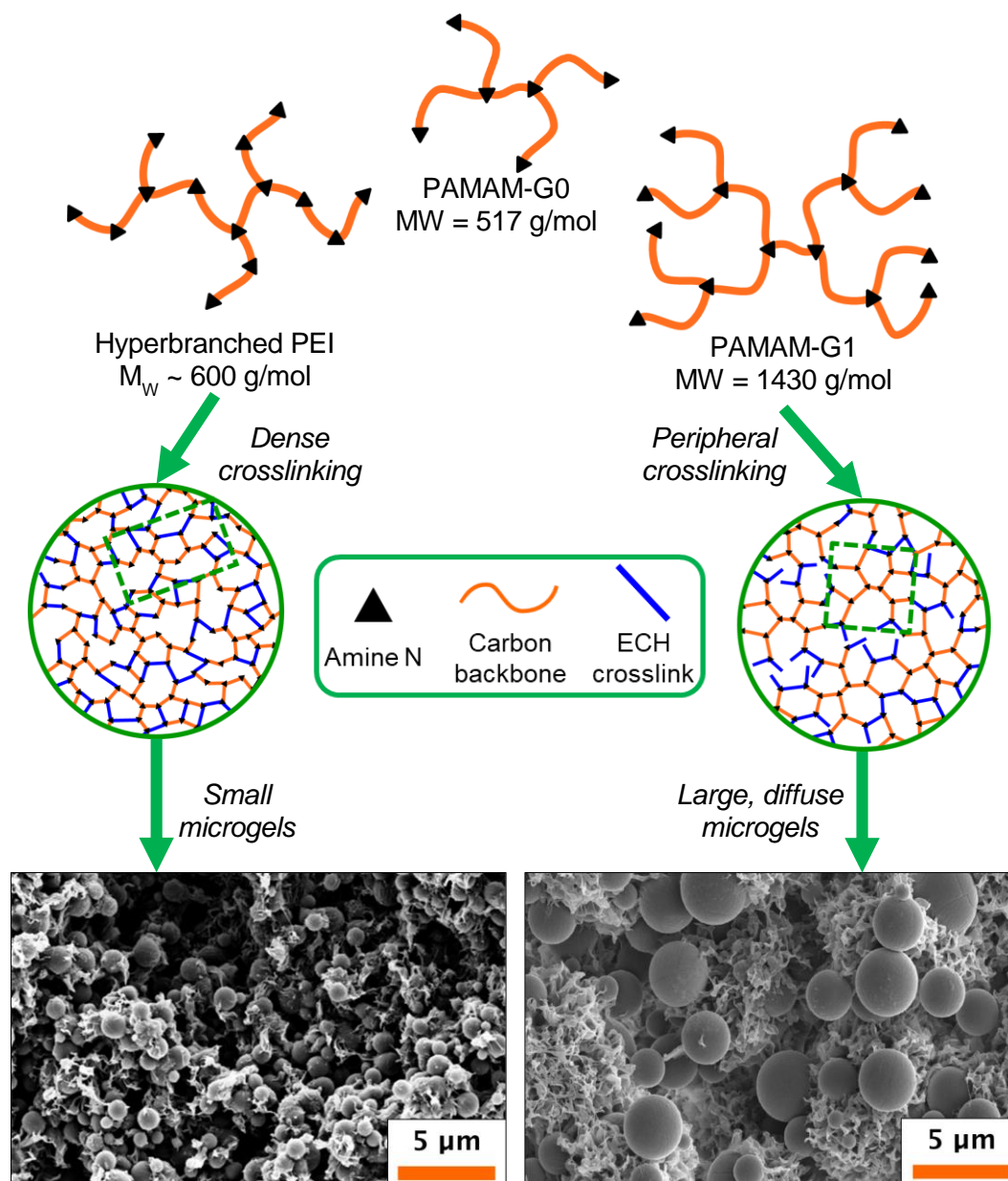
*Chapter III***POLYMER ARCHITECTURE PLAYS A CRUCIAL  
ROLE IN MICROGEL STRUCTURE FORMATION**

*Orland Bateman assisted with sample preparation, preliminary experiments, and USANS data collection detailed in this chapter. R.R.F designed the study, secured beamtime, prepared samples, and acquired & analyzed data.*

**III.1 Introduction**

With our method for measuring dynamic microstructure with ultra-small angle neutron scattering (USANS) established, we began to explore the relationship between microgel precursor and membrane structure. Specifically, we investigated the impact of dendritic architecture on the kinetics of crosslinking and phase separation, comparing samples with low-generation poly(amidoamine) (PAMAM) dendrimer as the precursor to those with randomly hyperbranched poly(ethyleneimine) (PEI) discussed in Chapter II. Cross sections of mixed-matrix polymeric particle (M2P2) membranes containing PEI- and G1-PAMAM-based microgels are compared in **Fig. III.1**, along with a proposed depiction to explain how precursor architecture can lead to divergent structures. All backbone amines of PAMAMs are tertiary, giving rise to the dendritic architecture. Consequently, the interior of the generally globular<sup>29</sup> polymer has no reactive sites for crosslinking by epichlorohydrin (ECH); only terminal amines are able to react to form microgels. The mesh spacing of the PAMAM-based microgel is effectively fixed and regular at the outset. On the other hand, the randomly hyperbranched PEI has a mixture of primary, secondary, and tertiary amines, with the former two both available for crosslinking. This leads to much denser microgels as epichlorohydrin (ECH) reacts both on the periphery and along the backbone of PEI. As is evident by the scanning electron microscopy (SEM) images in **Fig. III.1**, the architecture of the microgel precursor (dendrimer vs. hyperbranched) profoundly affects the size and number density of particles, despite being prepared under analogous conditions.





**Figure III.1:** Hypothesized effect of precursor architecture and chemical functionality on hierarchical structure and subsequent M2P2 membranes. Microgels derived from PEI are much smaller, with a greater number density in membranes leading to smaller and fewer PVDF-rich domains. Microgels from G1-PAMAM (right) are considerably larger, leading to membranes with much more pronounced PVDF-rich domains.

## III.2 Methods

### III.2.1 Preparation of USANS samples with PAMAM microgels

Neutron scattering samples were prepared for banjo (cylindrical) cells with 2 mm path length and 560  $\mu\text{L}$  capacity (Hellma Analytics). Similar to the experiments in Chapter II, we used stock solutions of poly(vinylidene fluoride) (PVDF; Kynar 761, Arkema) and PAMAM (ethylene diamine core, Generation 0.0 or 1.0, Dendritech) at double their intended concentrations, in hydrogenous and deuterated NMP. Because PAMAM is stored and sold as a 20 wt.% solution in methanol, we diluted the requisite mass of PAMAM into NMP and rotovapped the mixture at mild temperature to remove as much methanol as feasible. Additionally, based on our prior experience, we combined all reagents in a vial prior to loading into the banjo cell—ECH and HCl included. Otherwise, USANS samples were prepared by the same procedure.

### III.2.2 Preparation of USANS samples with PAMAM+PEI microgels

Neutron scattering samples containing both G0-PAMAM and PEI were prepared by the same procedure as other USANS samples with the following exception. Prior to mixing the microgel precursor with PVDF, a 3:1 mixture of G0-PAMAM stock to PEI stock was prepared in a separate vial and allowed to equilibrate for several minutes at room temperature. Then, the microgel mixture was combined with PVDF stock in equal volumes as any other sample.

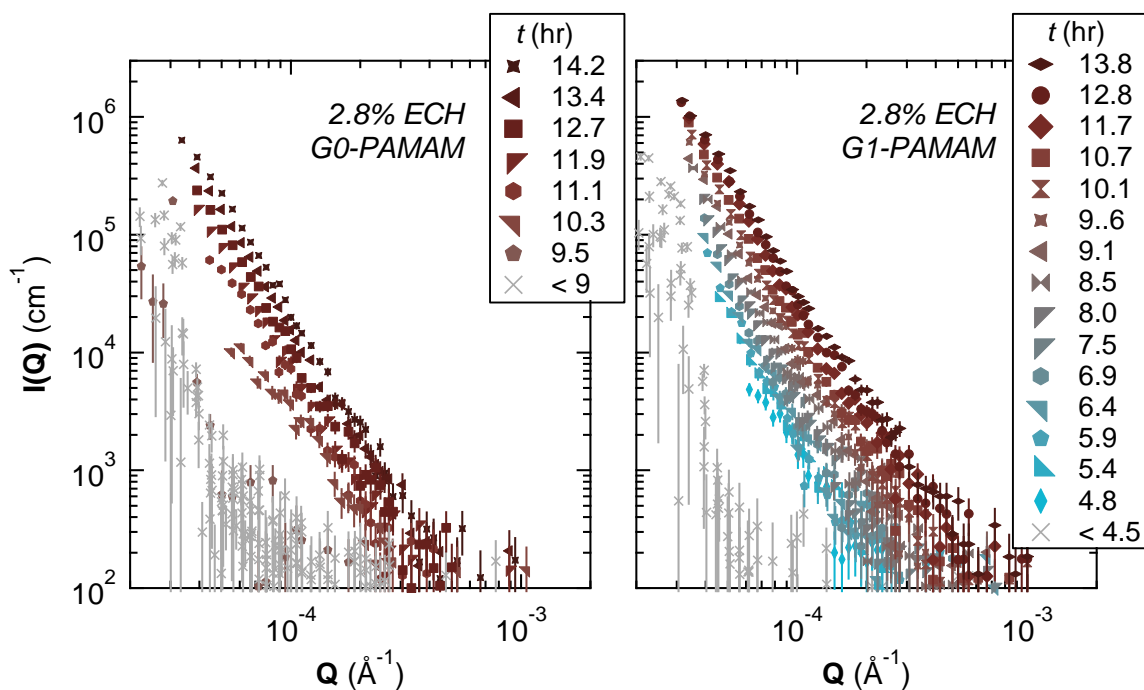
### III.2.3 Ultra-small angle neutron scattering experiments

USANS measurements were conducted on the BT5 Perfect Crystal Diffractometer at the NCNR, with incident beam wavelength of 2.38  $\text{\AA}$  and 6%  $\Delta\lambda/\lambda$  (FWHM) and  $\sim 17,000$  neutrons/ $\text{cm}^2\text{s}$  current at sample. The monochromator and analyzer are triple-bounce Si(220) crystals. Transient USANS experiments were conducted in two beamtime allocations, one in February 2016 and one in February 2019. The analyzer accepts a solid angle of  $7.1 \times 10^{-7}$  sr and has a slit height of  $0.117 \text{\AA}^{-1}$  in reciprocal space.

### III.3 Results & Discussion

#### III.3.1 Macrophase separation of PAMAM microgels

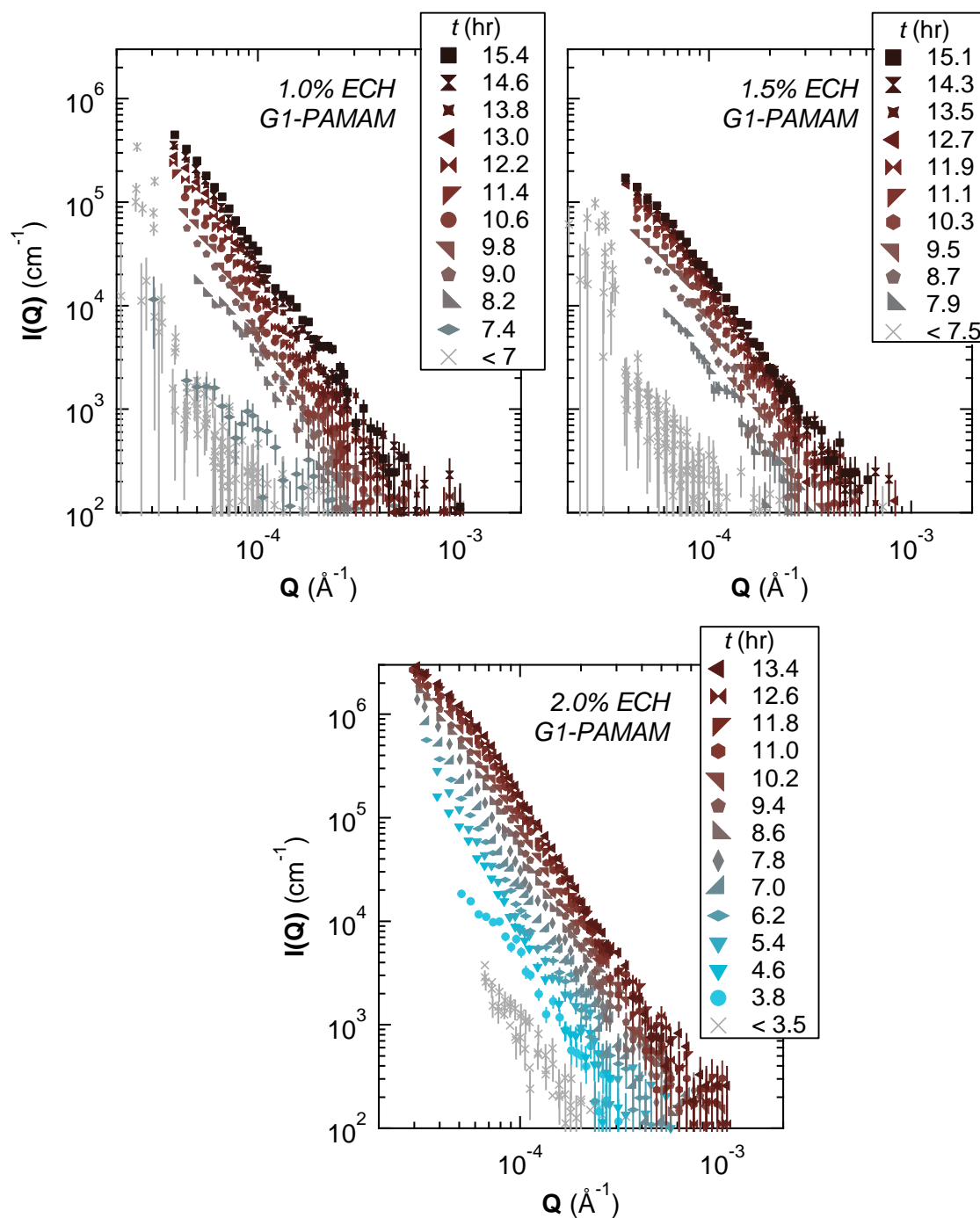
Time-resolved USANS patterns revealed that microgel architecture profoundly affects structure formation (**Fig. III.2**). While *in situ* microgel synthesis with PEI quickly plunges the system into the spinodal regime, casting solutions containing PAMAM develop structure much more slowly. In a casting solution containing 4% PAMAM-G0 (**Fig. III.2**, left), the latent period during which no structure has formed in the USANS lengthscale exceeds ten hours, followed by a modest growth in intensity that drifts to larger lengthscales than USANS probes. Latent periods in M2P2 casting solutions containing G1-PAMAM microgels are shorter than those with G0-PAMAM (**Fig. III.2**, right), but still appreciably longer than PEI-microgel solutions reported in Chapter II.



**Figure III.2:** Time-resolved USANS patterns from samples with PAMAM as the microgel precursor were markedly different from casting solutions with PEI. Moreover, the phase separation kinetics from G0-PAMAM are significantly slower than those from G1-PAMAM. Samples are in 100% deuterated NMP.

The time dependence of scattering profiles in PAMAM-containing M2P2 casting solutions suggests a nucleation and growth mechanism of phase separation; the long latent period is consistent with waiting for nucleation events to occur as the system resides in the metastable region of the phase diagram. A nucleation and growth mechanism agrees with SEM images showing much larger, more diffuse PAMAM particles compared to PEI (**Fig. III.1**). We hypothesize that the fixed internal mesh spacing of PAMAM-based microgels allow PVDF chains to maneuver and diffuse through microgels, allowing the system to undergo large scale phase segregation. Notably, in typical M2P2 membrane fabrications, large scale phase separation is prevented in the more concentrated solutions (~20 wt% total polymer) by mechanical stirring.

M2P2 solutions with G1-PAMAM and a range of concentrations of ECH are shown in **Fig. III.3**. Similarly to PEI, the effect of crosslinker concentration on the overall intensity of scattering is pronounced. However, unlike solutions with PEI, much higher concentrations of ECH and much longer reaction times are needed for scattering from PAMAM-microgels to surpass background. As with all other PAMAM-microgel solutions, the scattering patterns entail a single power law functional form, with object size exceeding the USANS window of lengthscales. A possible explanation for the substantially different scattering patterns for PAMAM casting solutions lies in the analytical technique: the deviations from a standard M2P2 membrane recipe—necessary to probe evolving structure with USANS—could be changing the mechanism and kinetics of microgel synthesis in PAMAM-containing casting solutions.

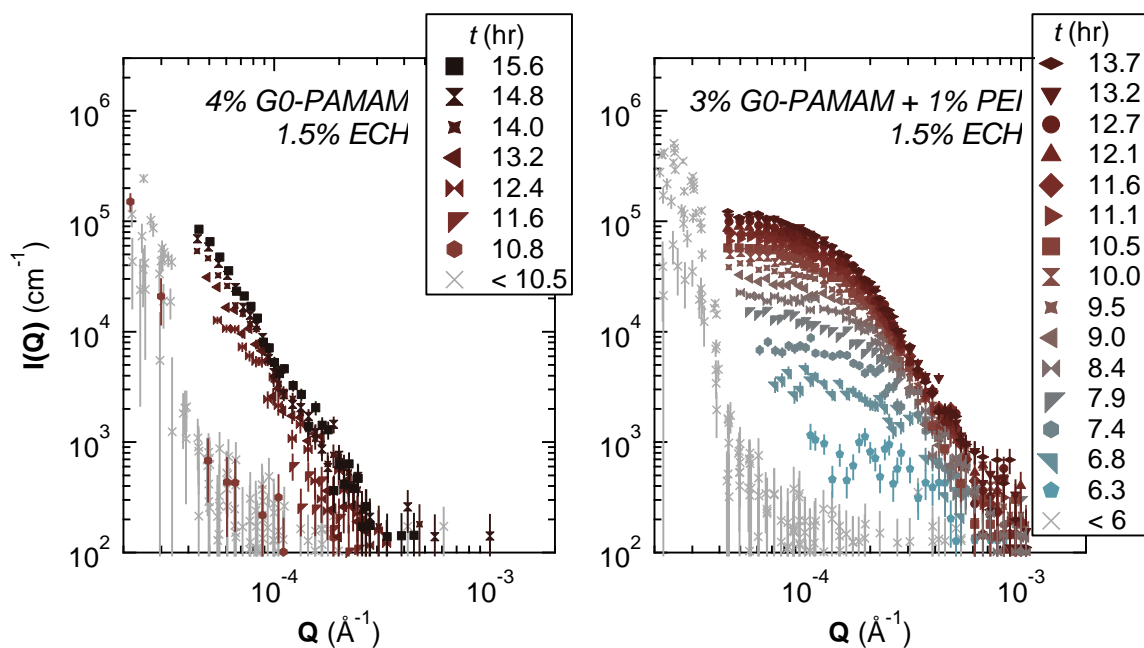


**Figure III.3:** Time-resolved scattering patterns with G1-PAMAM as the microgel precursor exhibit much slower kinetics than PEI precursors. Samples are in 100% deuterated NMP.

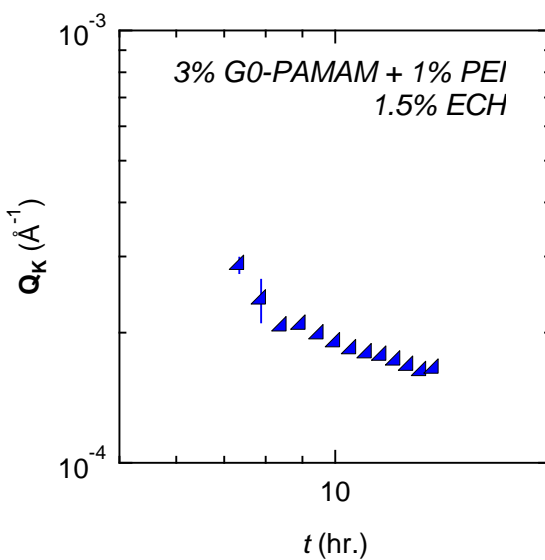
### III.3.2 Combination of PAMAM and PEI in M2P2 casting solutions

When G0-PAMAM is the nitrogen-rich precursor (**Fig. III.2**, left), the system proceeds into macroscopic phase separation—indicated by power law scattering extending beyond the USANS Q-range, and confirmed by visual observations and average particle size in SEM images. We hypothesized that a relatively small fraction of PEI introduced into the PAMAM microgel system might yield PAMAM-PEI microgels that avoid this macrophase separation. Indeed, replacing just a quarter of the G0-PAMAM with PEI causes drastically different features to emerge (**Fig. III.4**). Despite PEI being the minority nitrogen-containing constituent, the solution produces scattering patterns and domain sizes much more like those of PEI alone than of PAMAM alone. For functional membranes, the more finely distributed microgels are desired and the combination of amide and amine groups provided by PAMAM enable selective metal binding, motivating further investigation of the effect of PEI on morphology development in a PAMAM-precursor casting solution.

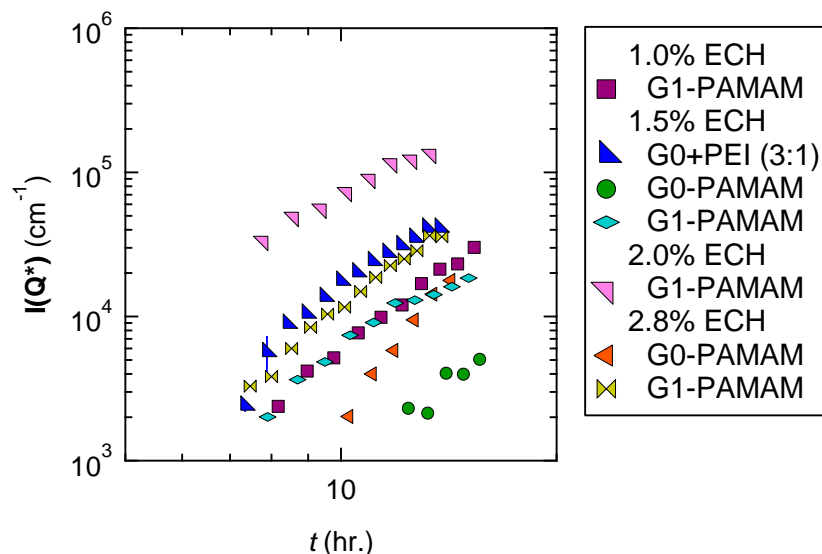
With the domain size back in the USANS range, we identified features and evaluated their time dependence using Kratky plots, by the same methods discussed in Chapter II. The resultant Kratky plot peak position,  $Q_K$ , for the casting solution containing hybrid PAMAM+PEI microgels, is shown in **Fig. III.5**. To compare the change in intensity at this characteristic wavevector to the time dependence of PAMAM-only microgel samples, we fit PAMAM scattering patterns to a power law, across the full Q-range of USANS. We then chose a Q value close to that of  $Q_K$ , denoted  $Q^*$ , of  $1 \times 10^{-4} \text{ \AA}^{-1}$  (**Fig. III.6**).



**Figure III.4:** Replacing a quarter of GO-PAMAM with PEI drastically changes the resulting domain size and phase separation kinetics of the casting solutions.



**Figure III.5:** Change in  $Q_K$  with reaction time in a PAMAM+PEI hybrid microgel M2P2 solution. In accordance with the time dependence observed for PEI-only casting solutions, we see an initial reduction in  $Q_K$  as domains are growing in size. At longer times, this decrease in  $Q_K$  tapers out, while intensity continues to grow steadily. For  $t < 9$  hrs.,  $Q_K \sim t^{-2.4}$ . For later times, the power law exponent approaches -0.5.



**Figure III.6:** To compare the rates of intensity growth for M2P2 casting solutions containing PAMAM-only microgels, scattering profiles were fit to a power law and  $Q^*$  was set to  $1 \times 10^{-4} \text{ \AA}^{-1}$ . For the casting solution with hybrid G0-PAMAM+PEI microgels, the peak of the Kratky plot was determined as described in Ch. II and used instead of  $Q^*$ .

### III.4 Summary

The divergent crosslinking kinetics between PEI and PAMAM clearly effect appreciable differences in domain size of M2P2 membranes. Preliminary data have indicated that the combination of PAMAM-G0 and a small amount of PEI in casting solutions leads to unusual phase behavior: characteristic lengthscales develop which are comparable to casting solutions with PEI-only microgels, but with kinetics similar to solutions with PAMAM-only microgels. More experiments are needed to fully understand how relative concentrations of PEI and PAMAM impact membrane morphology and performance. Ultimately, our results indicate that polymer architecture provides a utile handle to systematically tune M2P2 membrane structure, enabling facile tailoring to various applications.



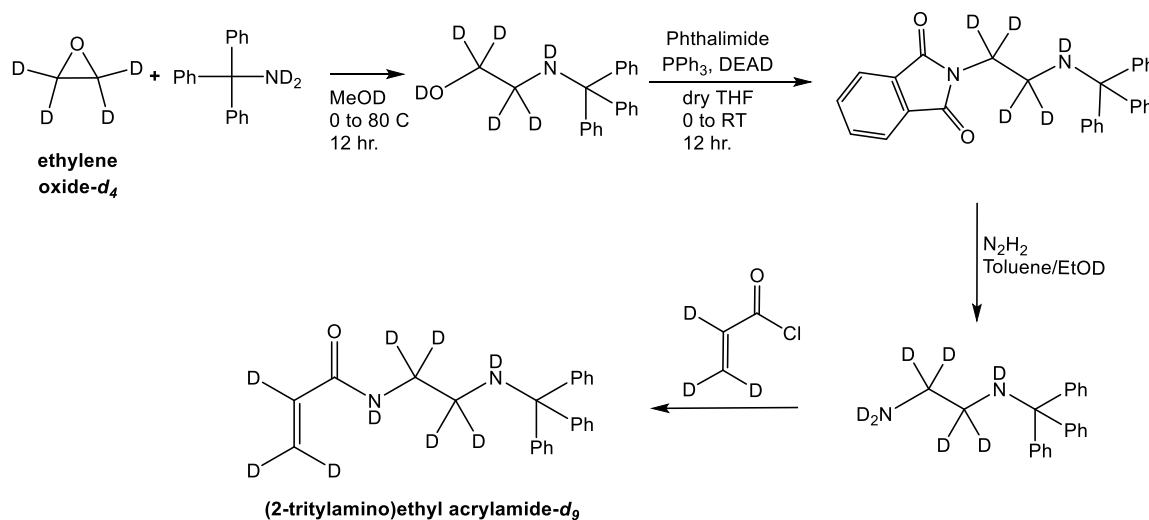
*Chapter IV***CONCLUSIONS AND OUTLOOK****IV.1 Key Findings and Implications for Membrane Design**

The specific features that make M2P2 membranes such a powerful tool in membrane science also impose substantial limitations on analytical techniques that probe how structure, precursors, and performance are fundamentally related to one another. The *in situ* synthesis of microgels plunges the system into a metastable or unstable regime, which then kinetically traps the structural polymer—creating otherwise unattainable structures while introducing significant physical complexity into the system. In our pursuit of understanding phase behavior in M2P2 membranes, we have developed a new analytical technique for characterizing evolving microstructure with USANS, which has applications to a vast array of research problems across geology, colloid science, biology, and materials science. Furthermore, we discovered an avenue to systematically tune the characteristic domain size in M2P2 casting solutions, by combining microgel precursors with different architecture and chemical reactivity.

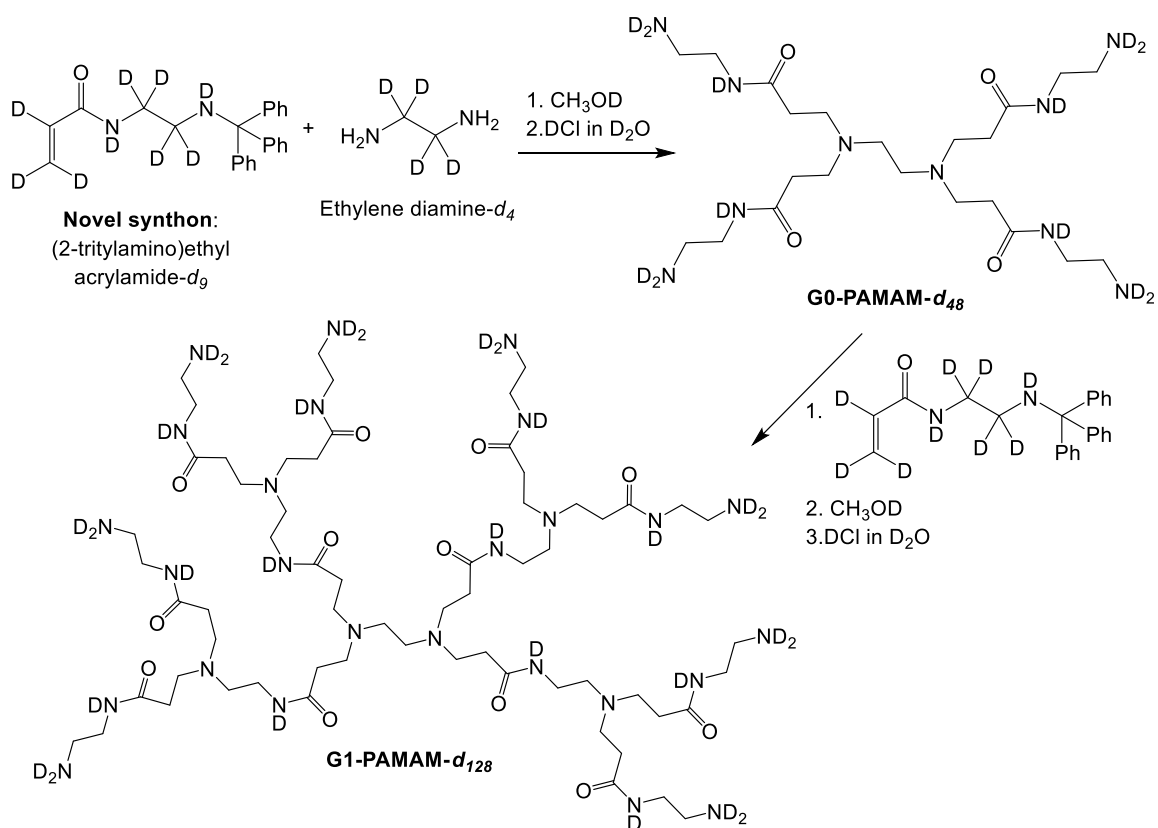
**IV.2 Future Work: Synthesis of Deuterium-labelled PAMAM Dendrimers**

Unanswered questions remain surrounding the contributions of each component in M2P2 casting solutions, and how they specifically impact performance of the resulting membrane. Contrast matching experiments with deuterium-labelled constituents can provide much-needed detail into how polymer architecture controls phase behavior in casting solutions, taking full advantage of all neutron scattering has to offer. We opted to target deuterated PAMAM for this

purpose. The traditional synthesis of PAMAM is termed the “Excess Reagents Method;” in order to prevent cyclic defects during synthesis, one key reagent—ethylene diamine—is used in a 50-fold excess<sup>30</sup>. In addition to being generally wasteful, this method becomes prohibitively expensive when using deuterated reagents. Therefore, Peter Bonnesen and Kunlun Hong of the Oak Ridge National Lab Center for Nanophase Materials Sciences devised a synthetic route to perdeuterated PAMAM dendrimers using a key protected acrylamide intermediate (**Fig. IV.1**)<sup>64</sup>. With deuterated PAMAM dendrimers, we can isolate the scattering contributions of PEI, PAMAM, and PVDF in casting solutions with hybrid microgels, and further interrogate phase behavior in membranes with PAMAM-only microgels.



**Figure IV.1:** Published synthesis of acrylamide synthon from deuterated ethylene oxide<sup>68</sup>. The limiting step is the introduction of the deuterated acryloyl group: in addition to being highly corrosive, acryloyl chloride is prone to homopolymerization.



**Figure IV.2:** Proposed synthesis of perdeuterated PAMAMs through a novel protected acrylamide synthon, proceeding to G1-PAMAM- $d_{128}$ .

*Appendix A*

## NEUTRON SCATTERING INSTRUMENTATION & DATA REDUCTION

### A.1 Introduction to Neutron Scattering

Small angle and ultra-small angle neutron scattering (SANS and USANS, respectively) techniques measure the scattering of a collimated neutron beam upon interaction with matter, to probe lengthscales in the range of 1 nm up to 20  $\mu\text{m}$ <sup>51,65</sup>. Isotropic spherical scattered neutrons from two different nuclei intersect at a given angle and a given distance from the sample, to generate a fringe pattern of bright and dark areas. The fringe pattern is a Fourier transform of nuclei positioning and ordering in real space, with distance between bright spots being inversely related to the distance between scattering nuclei. Thus, smaller scattering angles correspond to larger distances between nuclei. The reciprocal scattering space has as its independent variable the scattering wavevector,  $Q$ , which is related to angle by the following relation:

$$Q = \frac{4\pi}{\lambda} \sin \frac{\theta}{2} \dots\dots\dots (1)$$

where  $\theta$  is the scattering angle and  $\lambda$  is the wavelength of the incident neutron beam in  $\text{\AA}$ . At small angles measured in SANS and USANS,  $Q$  is approximated as  $2\pi\theta/\lambda$ . The shape of the scattering pattern can reveal such information as correlation lengths, radii of constituents, self-similarity (*i.e.* mass and surface fractals), and inter-particle structure in a sample. The information provided by small angle scattering in general is often complementary to microscopy techniques.

A unique advantage of neutron scattering is the ability to alter the scattering contributions of constituents by isotopic labelling. The differential scattering cross section of neutrons,  $\frac{d\Sigma}{d\Omega}$ , is dictated by the neutron scattering length,  $b$ . Scattering length is a fundamental property specific to each isotope of each element, and depends on both the neutron-nucleus interaction parameter and the nuclear radius of the isotope. Hence, the approximate doubling of nuclear radius between hydrogen and deuterium gives rise to significantly different scattering lengths for the two isotopes:  $b_H = -3.739$  fm while  $b_D = +6.671$  fm<sup>51</sup>. This makes deuterium labelling an effective method for isolating the structural contributions of individual species in a multicomponent sample.

The neutron scattering propensity for whole molecules is described as the scattering length density,  $\rho$ —a value calculated from the scattering lengths of the constituent atoms and the specific volume of the molecule.

$$\rho = \frac{N_A}{v} \sum_i n_i b_i \times 10^{-16} \text{ cm}^2/\text{\AA}^2 \dots\dots\dots (2)$$

where  $N_A$  is Avogadro's number,  $v$  is the specific volume in  $\text{cm}^3\text{mol}^{-1}$ , and  $n_i$  and  $b_i$  are the number of atoms and scattering length, respectively, for elemental constituent  $i$  in the molecule. For polymers, the scattering length density refers to the monomer rather than the entire macromolecule. The general scattering intensity,  $I(Q)$ , is given by

$$I(Q) = \frac{d\Sigma(Q)}{d\Omega} = \Delta\rho^2 V_p \phi S(Q) P(Q) \dots\dots\dots (3)$$

where  $\Delta\rho^2$  is the contrast factor (the square of the difference in  $\rho$  for the scattering particle and the continuum),  $V_p$  is the volume of a single scattering particle, and  $\phi$  is the volume fraction of the scattering particles in the sample. The inter-particle interactions are described

by the structure factor,  $S(Q)$ , while the intra-/single-particle structure is given by the form factor,  $P(Q)$ . At the low- $Q$  limit, the structure factor dominates the scattering; at the high- $Q$  limit, the form factor dominates.

## A.2 Data Reduction and Correction

Data reduction and correction are the processes by which raw output from a small angle scattering instrument is converted to absolute units ( $\text{cm}^{-1}$ ), enabling direct comparison to corrected data from other instruments. Specifically, the raw scattering angle is converted to wavevector  $Q$ , raw detector counts are scaled according to the incident intensity of the beam, any defects in the detector are accounted for, and normalized counts are converted to units of  $\text{cm}^{-1}$ . For SANS instruments at the NIST Center for Neutron Research (NCNR), detector counts are normalized to  $10^8$  monitor counts and then reduced by the following formula<sup>44</sup>:

$$I_{red}(Q) = \frac{I_{sam}(Q) - I_B}{T_{sam}} - \frac{I_{emp}(Q) - I_B}{T_{emp}} \dots\dots\dots (4)$$

where  $I_{sam}$  denotes the measured sample scattering,  $I_{emp}$  denotes the empty cell scattering,  $B$  denotes the blocked beam,  $T_{sam}$  denotes sample transmission, and  $T_{emp}$  denotes empty cell transmission. The empty cell scattering,  $I_{emp}(Q)$ , is measured while the blocked beam is a  $Q$ -independent constant that characterizes the electronic noise of the detector. Finally, the transmission-scaled data are converted to absolute intensity by:

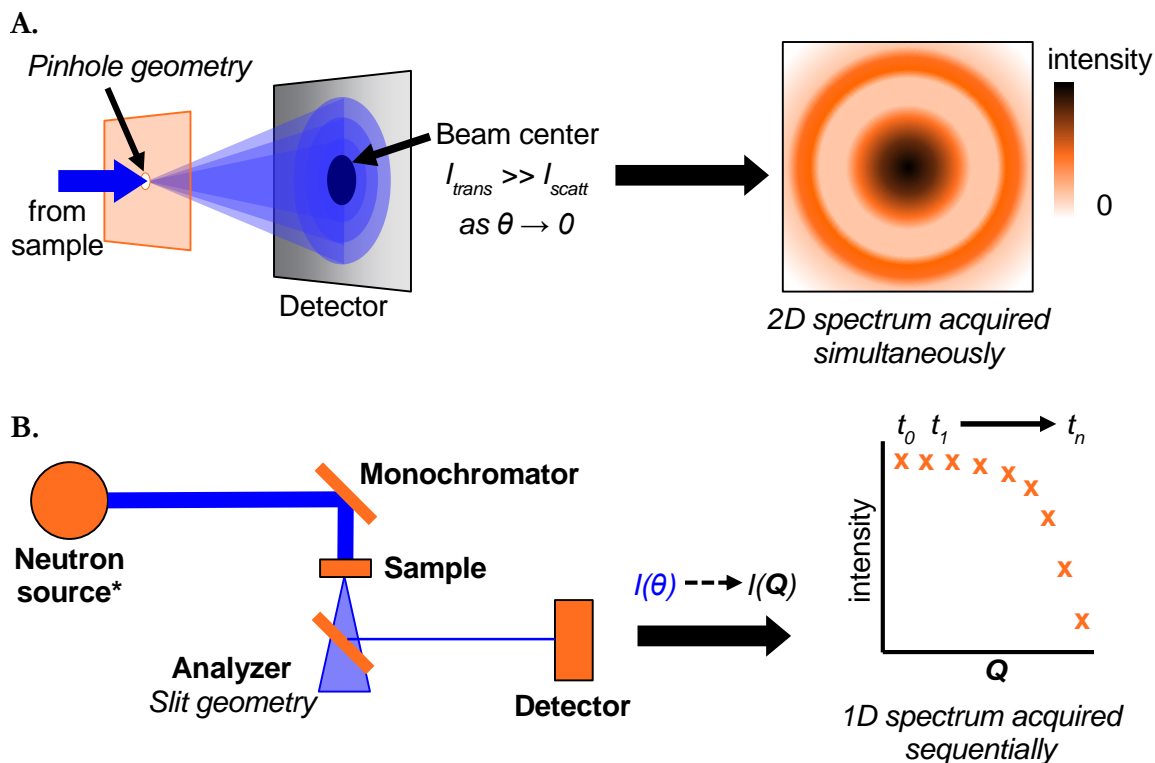
$$\frac{d\Sigma(Q)}{d\Omega} = \frac{I_{red}(Q)}{I_0(\lambda)T(\lambda)d_s\Delta\Omega} \dots\dots\dots (5)$$

where  $I_0(\lambda)$  is the transmission of the neutron beam without anything in the sample chamber,  $T(\lambda)$  is the sample transmission,  $\Delta\Omega$  is the solid angle in steradians, and  $d_s$  is the sample path length in cm.

## A.3 Specific Considerations for USANS

### A.3.1 Instrumentation and data acquisition

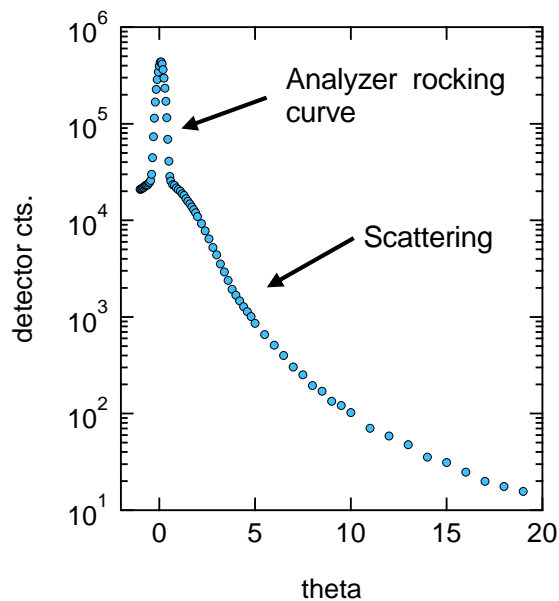
While a standard pinhole geometry and 2D detector offer sufficient angular resolution for SANS based on radial binning of pixels, the extremely small angles corresponding to microscale structure mandate different optics for USANS instruments (**Fig. A.1**)<sup>37,38</sup>. Using a rotating analyzer crystal paired with a stationary monochromator crystal (with sample situated between them), USANS instruments acquire a scattering pattern by sweeping through the full angular range sequentially (including the beam center to precisely determine  $Q=0$  for each measurement; **Fig. A.1 & A.2**). The angular range is segmented into "buffers"—subsets of angles—dictated by the signal-to-noise (S/N), which inherently decays as you move further from the beam center (the opposite trend of SANS intensities/acquisition times). To preserve comparable S/N across the full angular range, while keeping the total acquisition time within reason, each buffer has different spacing between angles of acquisition, called the  $\theta$  step, and adjustable acquisition time for the points in that buffer. For the BT5 Perfect Crystal Diffractometer at the NCNR, the acquisition parameters for buffers are defined by the time spent acquiring at each angular point.



**Figure A.1:** Scattering instruments with different geometries. **A.** The pinhole geometry utilized in most SANS instruments enables the simultaneous collection of the 2D pattern. **B.** The Bense-Hart USANS instrument uses a rotating analyzer crystal with slit geometry such that a single scattering angle is transmitted to the detector at a time. The raw data is inherently 1D, as the pattern is acquired incrementally. Not to scale.

\*The neutron beam undergoes a series of collimation and focusing prior to reaching the monochromator, which is not shown.





**Figure A.2:** Representative USANS scattering pattern showing the rocking curve and sample scattering. The rocking curve is used to set  $Q=0$  and determine the transmission of the

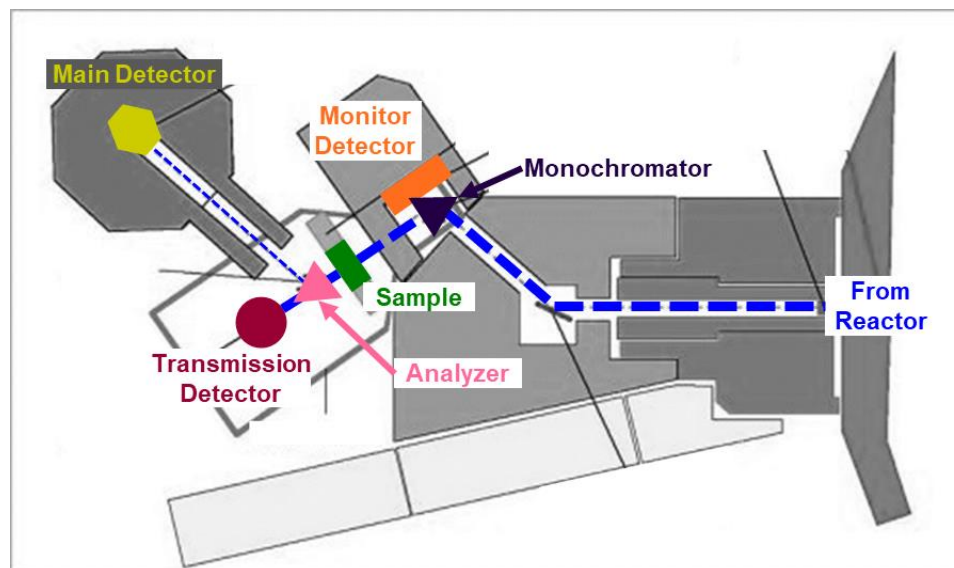
To ensure precise measurement of  $Q$  at such small angles of USANS, the analyzer crystal begins at negative angles and sweeps through the rocking curve of the crystal—the beam center—within each USANS measurement (**Fig. A.2**). During data reduction,  $Q=0$  is determined by fitting the eleven points closest to the raw maximum intensity (five to the left and five to the right of  $Q_{\max}$ ) to a Gaussian distribution. While NIST provided macros written for USANS data reduction and correction in Igor Pro<sup>44</sup>, we merely used the USANS Reduction Panel to interpret raw .bt5 files and export as a .txt file; we wrote python programs to perform subsequent data reduction and correction.

After raw files are processed to I vs. Q data sets and detector counts are normalized to  $10^6$  monitor counts (note the discrepancy with SANS normalization), USANS data are reduced the following formula:

$$I_{red}(Q) = I_{sam}(Q) - T_{Rock}I_{emp}(Q) - (1 - T_{ROCK})I_B \dots\dots\dots(6)$$

where  $T_{Rock}$  is  $I_{sam}(Q = 0)/I_{emp}(Q = 0)$ , the transmission measured as the rocking curve;  $I_{sam}(Q = 0)$  is analogous to  $T_{sam}$  and  $I_{emp}(Q = 0)$  is analogous to  $T_{emp}$  of the SANS reduction formula (Eqn. 4). The remaining terms are equivalent to those in Eqn. 4; for the BT5 USANS instrument,  $I_B$  is 0.62. (Note: The missing  $1/T_{sam}$  term [*i.e.*  $1/I_{sam}(Q = 0)$ ] of Eqn. 4 is included in the correction formula to convert counts to  $\text{cm}^{-1}$ ). Another transmission term is used in lieu of  $\{I_0(\lambda)T(\lambda)\}$  of Eqn. 5, called  $T_{Wide}$ . This parameter is based on measurements of the dedicated transmission detector (**Fig. A.2**), and is defined as the average transmission for  $\theta > 2$  (or  $Q > 1 \times 10^{-4} \text{ \AA}^{-1}$ , so-called wide angles) for the sample divided by that of the empty cell. Finally, reduced data are converted to absolute intensity by the formula:

$$\frac{d\Sigma(Q)}{d\Omega} = \frac{I_{red}(Q)}{I_{sam}(Q=0)T_{Wide}d_s\Delta\Omega} \dots\dots\dots(7)$$



**Figure A.3:** Aerial view of the BT5 USANS instrument at NCNR, with key components highlighted as well as the neutron beam and scattering paths (blue dashed lines). Image schematic modified from the instrument website, converted to gray scale for simplicity:

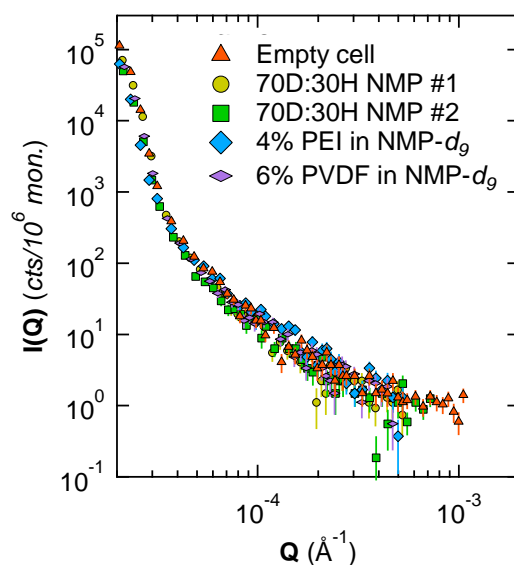
<https://www.ncnr.nist.gov/equipment/msnew/ncnr/bt5-usans-ultra-small-angle-neutron-scattering.html>

### A.3.2 Quantitative determination of the Q-dependent background

Deviating from the standard NCNR reduction protocol for USANS, in which an empty cell measurement is subtracted from the sample scattering (Eqn. 6), we sought to determine an accurate, smooth function for the Q-dependent background scattering, so that subtracting the background neither skewed the data nor introduced additional noise. We deemed this extra measure necessary because our time-resolved data contained far more noise and, at short reaction times, far lower sample scattering than the conventional USANS measurement.

To this end, we considered samples that contained at most one polymer + solvent; PVDF and PEI each lack structure in the lengthscale probed by USANS, making those samples effectively blanks. Visual inspection of the plotted data for these samples confirmed this notion: they were indistinguishable from the empty cell measurement (**Fig. A.4**). Five

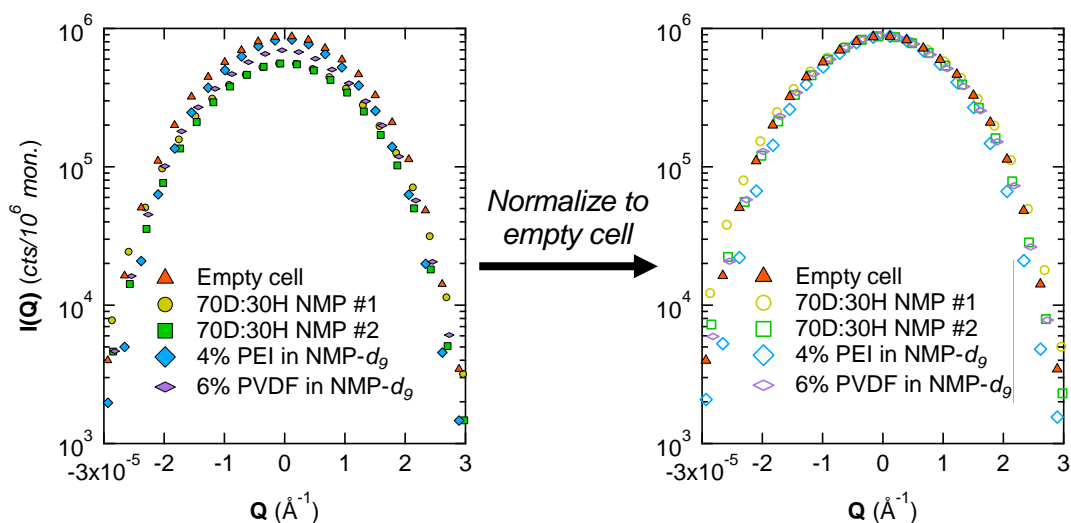
samples met this criterion and passed visual inspection: (i) the empty cell, (ii, iii) two replicate measurements of 70D:30H-NMP, (iv) 4.2% PEI in fully deuterated NMP, and (v) 6.1% PVDF in deuterated NMP. We refer to this set of samples as “blanks.”



**Figure A.4:** Scattering of the five "blanks" from the February 2016 experiment. One physical sample was measured twice, 70% deuterated NMP.

There are a few reasonable options by which to proceed in terms of considering all five blanks as measurements of the same scattering pattern, that is, the  $Q$ -dependent background. The five samples could be merged into single array of  $I$  vs.  $Q$  and then smoothed or fit to a function, though the peaks have some variance in both maximum intensity and in beam width (**Fig. A.5**). Alternatively, the five samples could be normalized to some maximum intensity prior to merging and then smoothing/fitting. We have two overall goals: (i) accurately capture the behavior within the  $Q$ -range where scattering is distinguishable from the rocking curve, and (ii) preserve the transmission information contained in the beam center, for reduction by Eqn. 6. Therefore, in pursuit of the second goal, we normalized blanks according to the peak intensity of the empty cell,  $8.76 \times 10^5$ , **Fig. A.5**, and then merged the five blanks into a single  $I$  vs.  $Q$  data set. Combining the constituent measurements serves to improve reliability of the fit in the high- $Q$  regime, while normalization provides a clean, uniform beam

center. (Note: A simple average of the five blanks is not feasible as the precise  $Q$  values of the data are not conserved across measurements, as opposed to SANS radial binning of 2D raw data to generate the same set of  $Q$  values for every measurement.)



**Figure A.5:** Effect of normalization on blanks at the beam center. Peak intensity was determined by fitting to a Gaussian peak; all blanks were normalized to the peak intensity of the empty cell.

Following the combination of blanks into a single data set, we sought to determine the incoherent background scattering term (called the EMP LVL in the NCNR USANS correction panel for Igor Pro). We fit the merged blanks to a power law for  $Q > 1 \times 10^{-4} \text{ \AA}^{-1}$  (**Table A.1**). The beam center of the merged data set was then fit to a Gaussian peak to ascertain the peak width,  $B$ . For this fit,  $I_0$  was held at the normalization constant, the peak position was fixed at  $Q=0$ , and the incoherent scattering term was set according to the high- $Q$  result rounded to two significant digits (**Table A.1**).

**Table A.1:** Optimal fit parameters for incoherent scattering and beam width for merged blanks. Chi-squared fits performed using Igor Pro.

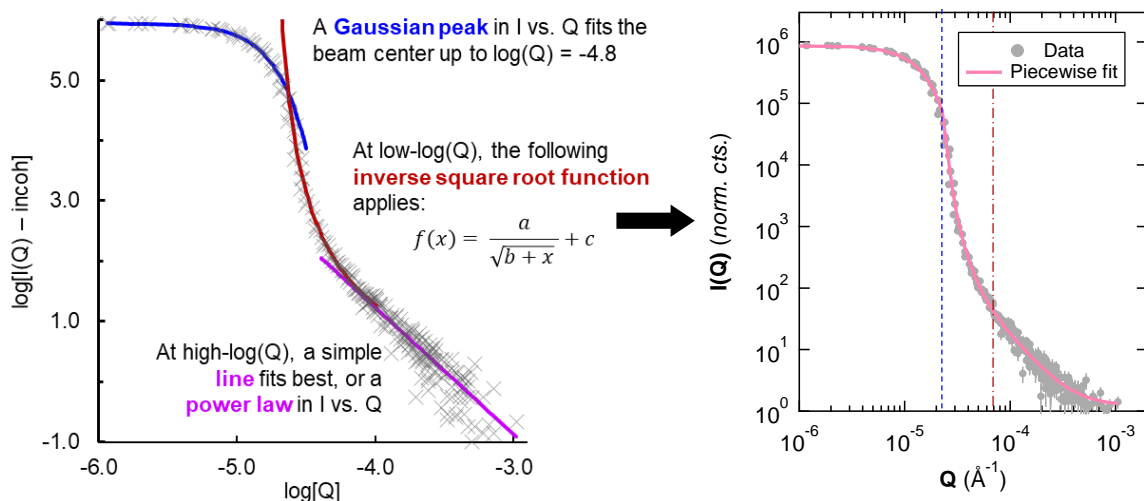
Model	Domain ( $\text{\AA}^{-1}$ )	Parameters	Value	Error	Fit statistic
Power law	$Q > 1 \times 10^{-4}$	m	2.330	0.146	$\chi^2 = 171$
		A	$8.23 \times 10^{-9}$	$1.07 \times 10^{-8}$	
		incoh	1.171	0.119	
Gaussian peak	$-2 \times 10^{-5} \leq Q \leq 2 \times 10^{-5}$	$I_0$	$8.76 \times 10^{+5}$	fixed	$\chi^2 = 62600$
		$Q_0$	0	fixed	
		B	$1.025 \times 10^{-5}$	$2 \times 10^{-9}$	
		incoh	1.2	fixed	

We then subtracted the incoherent scattering term, 1.2, from the combined blanks and took the log of  $\{I - \text{incoh}\}$  and  $Q$  for subsequent piecewise fitting using the method of maximum likelihood estimation (MLE). The Gaussian peak of the beam center follows the data up to  $Q = 1.6 \times 10^{-5} \text{\AA}^{-1}$ , while the power law only applies to high- $Q$  (**Fig. A.6**). We screened several functional forms for the low- $Q$  regime, seeking the simplest model that accurately captures the behavior. We concluded that an offset inverse square root functional form suited these needs best. The final piecewise fit for the  $Q$ -dependent background,  $I_{QDB}$ , is as follows:

$$I_{QDB}(Q) = f(Q) + 1.2 \dots \dots \dots (8)$$

where  $f(Q)$  is given by:

$$f(Q) = \begin{cases} 8.76 \times 10^5 \exp \left[ -0.5 \times \left( \frac{Q}{1.025 \times 10^{-5}} \right)^2 \right] & Q \leq 2.358 \times 10^{-5} \\ 0.02698 \times 10^{\frac{2.515}{\sqrt{4.784 + \log Q}}} & 2.358 \times 10^{-5} < Q \leq 8.511 \times 10^{-5} \\ 6.498 \times 10^{-8} Q^{-2.1046} & Q > 8.511 \times 10^{-5} \end{cases}$$



**Figure A.6:** Piecewise fit of the  $Q$ -dependent background scattering in samples from February 2016. Constituent functions include a Gaussian peak for the beam center, a power law at high- $Q$ , and an inverse square root function to bridge the two (**left**). The smooth piecewise function agrees well with the "blanks" data set in  $I$  vs.  $Q$ ; the transition between constituent functions is indicated with vertical dashed lines (**right**).

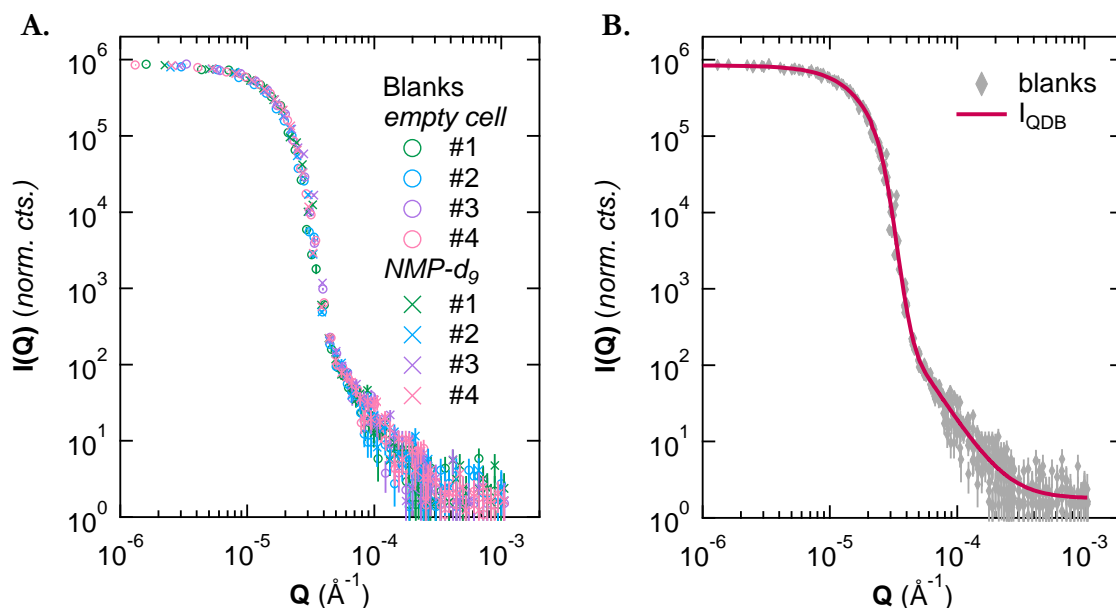
A similar process was used for the  $Q$ -dependent background in measurements from 2019, with some notable differences. Blanks composed of four replicate measurements each of one empty cell and one cell filled with NMP- $d_9$  taken over five days. The first three measurements for each physical blank were taken using 35 minutes of acquisition, while the fourth measurement for each blank used an acquisition time of 57 minutes. For the normalization constant, we chose the peak position of the longest empty cell measurement,  $8.45 \times 10^5$  cts./ $10^6$  monitor cts. Additionally, we judged that the best functional form for the low- $\log[Q]$  region bridging the Gaussian beam center with the high- $Q$  power law was a Sigmoid function rather than an inverse square root. The  $Q$ -dependent background for data collected in 2019 is on the following page.

$$I_{QDB}(Q) = f(Q) + 1.8 \dots \dots \dots (9)$$

where  $f(Q)$  is given by:

$$f(Q) = \begin{cases} 8.45 \times 10^5 \exp \left[ -0.5 \times \left( \frac{Q}{1.14 \times 10^{-5}} \right)^2 \right] & Q \leq 2.148 \times 10^{-5} \\ 10^{\left\{ \frac{-3.7762}{1 + \exp[-12.23(\log[Q] + 4.47)]} + 5.44 \right\}} & 2.148 \times 10^{-5} < Q \leq 5.662 \times 10^{-5} \\ 9.7364 \times 10^{-10} Q^{-2.5641} & Q > 5.662 \times 10^{-5} \end{cases}$$

Normalized constituent blanks and fit results are shown in **Fig. A.7**. The python program used to perform these Q-dependent background fits can be found in the CaltechDATA repository<sup>66</sup>.



**Figure A.7:** Q-dependent background for 2019 USANS experiments. **A.** Two physical blanks, an empty cell and NMP- $d_9$ , were measured over several days and normalized to the peak intensity of the fourth measurement of the empty cell. **B.** Merged blanks were fit to a piecewise function composed of a Gaussian peak, a Sigmoid function in logspace, and a power law.

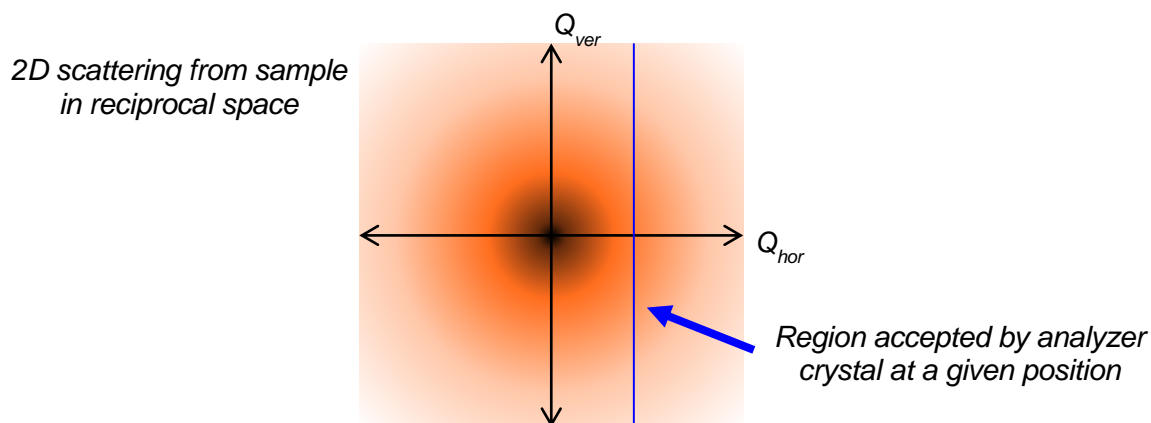


### A.3.3 Slit smearing

The slit geometry which affords the exquisite angular resolution of USANS bears a cost: scattering becomes smeared by the rectangular binning of the slit (**Fig. A.9**)<sup>43,51</sup>. The resulting smeared scattering  $I_{sm}(Q)$  is a convolution of the scattering function for the horizontal component,  $I_{hor}(Q)$ , and the resolution function  $R(Q_{ver})$ :

$$I_{sm}(Q) = \frac{1}{\delta Q_v} \int_{-\delta Q_v}^{+\delta Q_v} R(Q_{ver}) I_{hor}(\sqrt{Q_{hor}^2 + Q_{ver}^2}) dQ_{ver} \dots\dots\dots(11)$$

where  $\delta Q_v$  is the slit height in reciprocal (Q) space and  $R(Q_{ver}) = \delta Q_v$ . For the BT5 USANS instrument, the slit height is  $0.117 \text{ \AA}^{-1}$ .



**Figure A.8:** Effect of slit geometry for USANS instruments. Neutrons are scattered as spherical waves producing a fringe pattern with horizontal ( $Q_{hor}$ ) and vertical ( $Q_{ver}$ ) components in reciprocal space. The analyzer crystal accepts an effectively single angle in the horizontal direction but all angles of the vertical component, resulting in rectangular binning of the 1D scattering pattern.

If the "true" scattering (*i.e.* scattering in a single Q-direction) is a power law with no incoherent scattering term, the BT5 USANS smeared scattering pattern would instead be the following:

$$I_{sm}(Q) = 2A\delta Q_v Q^{-m} \times {}_2F_1\left(\frac{1}{2}, \frac{m}{2}; \frac{3}{2}; -\frac{\delta Q_v^2}{Q^2}\right) \dots\dots\dots (12)$$

where  ${}_2F_1$  is Gauss's hypergeometric function. The python program for smearing SANS data based on predetermined model parameters can be found in the CaltechDATA repository<sup>66</sup>.

### A.3.4 Distinguishing between background/beam and sample scattering

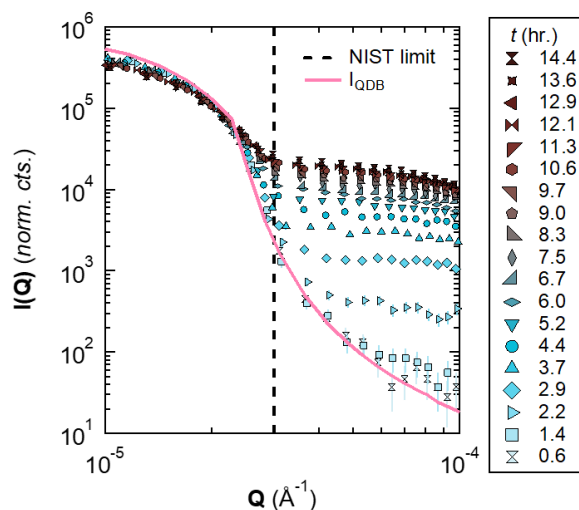
The limit of detection (LOD) in Q for time-resolved USANS data varies with reaction time and level of deuteration of the solvent (*i.e.*,  $Q_{LOD}$  varies with overall intensity of scattering at low-Q) (**Fig. A.9**). We determined that normalized counts as a factor of the Q-dependent background could serve as a suitable objective criterion for discriminating between background-dominated scattering and sample scattering. To this end, we define two parameters, individual ratio  $\mathcal{J}_n$  and five-point moving average  $\mathcal{A}_n$ , as follows:

$$\mathcal{J}_n = \frac{I_{red}(Q_n)}{I_{QDB}(Q_n)} \dots\dots\dots (10a)$$

$$\mathcal{A}_n = \frac{1}{5} \sum_{i=n-4}^n \mathcal{J}_i \dots\dots\dots (10b)$$

where  $I_{red}(Q)$  is the reduced intensity, (*i.e.* prior to correction), in detector counts per  $10^6$  monitor counts. We screened several methods for setting the Q-LOD based on  $\mathcal{J}_n$  and  $\mathcal{A}_n$  parameters, wherein  $Q_{LOD}$  is the minimum  $Q_n$  such that  $\mathcal{J}_n$  or  $\mathcal{A}_n$  exceeds a certain value. The results of this screen are shown in **Fig. A.10**, for a representative sample. The analogous method in SANS to eliminate data points for which the incident beam overwhelms any sample

scattering is the application of a mask onto the 2D pattern. In SANS at NIST, the mask also covers damaged or unreliable pixels in the detector (thus, specific to each instrument).

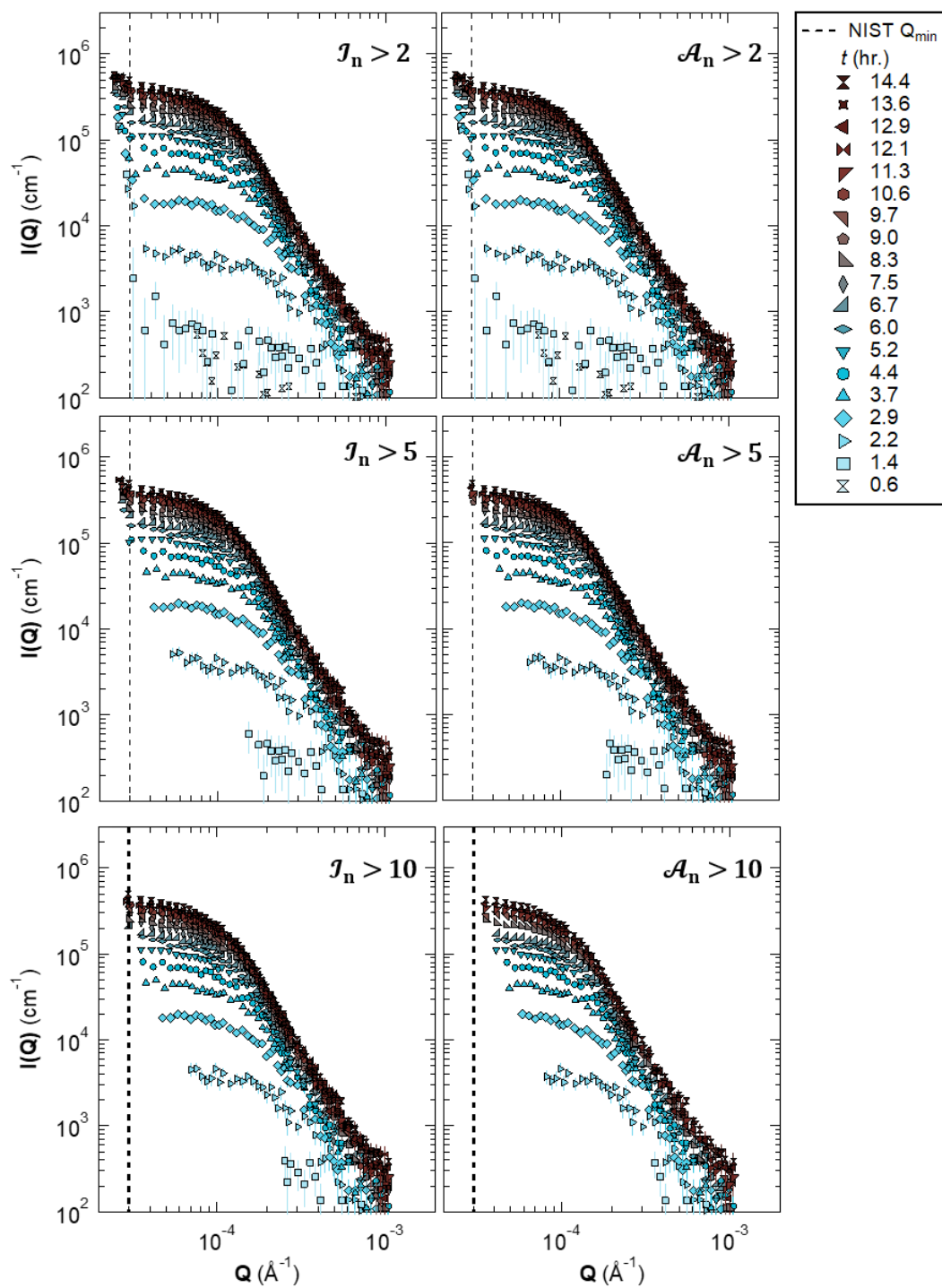


**Figure A.9:** Raw scattering data for a representative sample compared to  $I_{QDB}$ . The lowest  $Q$  value at which sample scattering deviates from background depends on the reaction time.

Normalized counts: detector counts per  $10^6$  monitor counts.

Sample composition: 6.1% PVDF, 4.2% PEI, 0.4% ECH, & catalytic HCl in NMP- $d_5$  (100% D).

We judged that the trimming criterion  $\mathcal{A}_n > 5$  strikes the best compromise between removing the all data influenced by the  $Q$ -dependent background, particularly for longer reaction times, without discarding too many points at the shortest times. Moreover, by choosing a moving average,  $\mathcal{A}_n$ , instead of the first individual occurrence of signal exceeding a factor of  $I_{QDB}$ , the method is less sensitive to random fluctuations in the scattering signal due to short acquisition times of time-resolved USANS. The python program used for the chosen trimming criterion,  $\mathcal{A}_n > 5$ , can be found in the CaltechDATA repository<sup>66</sup>.



**Figure A.10:** Removal of background-dominated data by applying various criteria related to sample scattering and the  $Q$ -dependent background, indicated in the inset of each plot.

## *Appendix B*

# METHOD OF FITTING & ANALYSIS

## B.1 Maximum Likelihood Estimation

The maximum likelihood estimator is a method for fitting data to a specified model based on the probability distribution of errors in the data set<sup>67</sup>. The optimal set of parameters,  $\{\Delta_{opt}\}$ , is found by maximizing the likelihood function, defined by a model,  $f(x; \{\Delta_k\})$ , and a probability distribution. Errors in USANS data follow a Poisson distribution

$$P(y_i; \lambda_i) = \frac{e^{-\lambda_i} \lambda_i^{y_i}}{y_i!} \dots\dots\dots(13)$$

where  $y_i$  is the observed data and  $\lambda_i = f(x_i; \{\Delta_k\})$ . The ‘‘Likelihood,’’  $\mathfrak{L}(\{\Delta_k\})$ , that the set of parameters  $\{\Delta_k\}$  describes the whole data set is the product of the individual probabilities:

$$\mathfrak{L}(\{\Delta_k\}) = \prod_i P(y_i; \lambda_i = f(x_i; \{\Delta_k\})) \dots\dots\dots(14)$$

Thus, the independent variables of the likelihood function are the parameter values; the set of model parameters most likely to give rise to the observed data is the maximum of the likelihood function  $\mathfrak{L}(\{\Delta_k\})$ . Finding the maximum of this product function is computationally taxing, so we take the natural log of both sides:

$$\ln[\mathfrak{L}(\{\Delta_k\})] = \ln\{\prod_i P(y_i; \lambda_i = f(x_i; \{\Delta_k\}))\} \dots\dots\dots(15a)$$

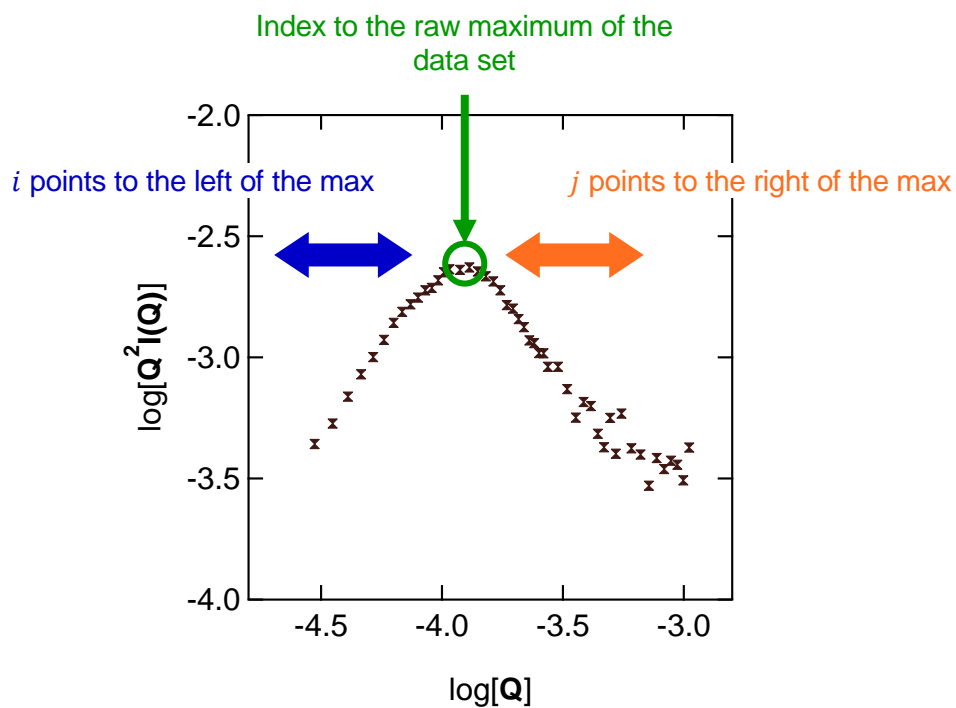
$$\therefore \ln[\mathfrak{L}(\{\Delta_k\})] = \sum_i \ln\{P(y_i; f(x_i; \{\Delta_k\}))\} \dots\dots\dots(15b)$$

Because all probabilities are constrained to the interval (0, 1), all logarithms exist and are negative. Therefore, the maximum of the summed logarithms occurs at the same point as the original likelihood product. In short, the likelihood function computes the overall probability of obtaining the entire observed data set as a function parameter values. As an aside, if errors are normally distributed, the MLE returns the same optimal set of parameters as ordinary least squares fitting<sup>67</sup>.

Whenever possible, we conducted fits using the MLE for two reasons. First, with scattering intensities spanning several decades,  $\chi^2$  is susceptible to bias in favor of minimizing error for high-intensity points at the expense of a poorer fit for lower-intensity regions. Second, MLE is easily tailored to weighting by different distributions of error, and the error in neutron scattering data is described by a Poisson distribution (Eqn. 13). We fit data in logspace because the factorial in the denominator of the Poisson distribution prohibits working in I versus Q; factorials become computationally impossible to work with around  $y = 270$ . The factorial term poses another problem when implementing MLE for data in logspace. Because  $\log[I(Q)]$  is constrained to  $[-1, 6]$ , the Poisson probabilities are significantly discretized. Therefore, in our MLE program, we multiplied the  $\log[I - \text{incoh}]$  and the corresponding model fit by ten—striking a compromise between computational feasibility and sensitivity to errors. The python program for a few representative MLE models with Poisson errors can be found in the CaltechDATA repository<sup>66</sup>.

## B.2 Determination of $Q_K$ from Kratky Plots

The Kratky plot,  $Q^2 \times I(Q)$  versus  $Q$ , is a means by which to graphically demonstrate power law scattering exponents and deviation therefrom<sup>51</sup>. Typically, Kratky plots are used in scattering from polymer solutions and the plot demonstrates whether the polymer behaves as a Gaussian chain ( $I \sim Q^{-2}$ ), indicated by a flat region in the Kratky plot. Here, we use the Kratky plot in a similar way: as a tool to identify features in our USANS scattering patterns.



**Figure B.1:** Kratky plot showing how the  $\log[Q]$ -regime of the peak was indexed and screened. We screened permutations of  $(i, j)$  pairs ranging from three to ten.

We concluded that fits over  $i$  values ranging 4 – 6 and  $j$  values ranging 7 – 9 provided the most stable peak positions, such that our specific choice of  $\log[Q]$ -subset does not impact the conclusions we draw from the results. We averaged the peak positions from the nine  $(i, j)$  fit ranges.

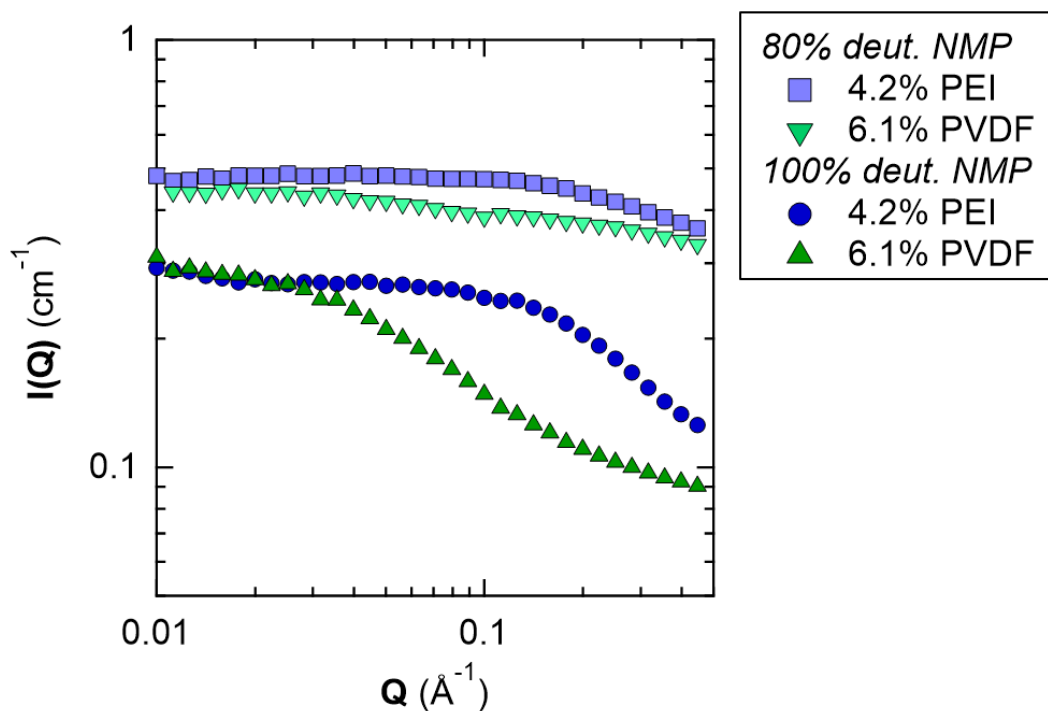
## *Appendix C*

### SUPPLEMENTARY DATA

#### C.1 Small-angle neutron scattering of Individual Polymers

For solutions containing 6.1 wt.% poly(vinylidene fluoride) (PVDF), the 400 kg/mol chains overlap appreciably: their  $R_g$  is 50 nm to give an overlap concentration,  $c^*_{\text{PVDF}}$ , of just 0.13%. However, for polyethyleneimine (PEI), the concentration used, 4.2 wt%, remains well below the overlap concentration ( $R_g < 2$  nm;  $c^*_{\text{PEI}} > 28\%$ ). Small-angle neutron scattering (SANS) patterns of PVDF solutions show stronger intensity variation with respect to PEI solutions because PVDF is at higher concentration and a single blob has more scattering centers than a PEI molecule (**Fig. C.1**). These effects are offset by the fact that PVDF has lower contrast in scattering length density ( $\rho_{\text{PVDF}} = 2.86$  and  $\rho_{\text{NMP-d9}} = 6.71$ ; scattering power scales as the square of the difference) than that of PEI ( $\rho_{\text{PEI}} = 0.56$ ). The scattering by each of the two polymers is reduced by using a mixture of 20% hydrogenous NMP with 80% deuterated NMP. This mixture, denoted 80D:20H-NMP, has  $\rho_{80\text{dNMP}} = 5.55$ ; the effect being stronger for PVDF than for PEI (compared to the polymers in fully deuterated NMP, the contrast of PVDF is reduced by 56% while the contrast for PEI is only reduced by 34%). The absolute scattering appears higher due to the incoherent scattering contribution of the hydrogens in hNMP. When the incoherent scattering of  $0.33 \text{ cm}^{-1}$ , approximately independent of  $Q$ , is added to the product of the contrast ratio and the scattering pattern observed from polymers in 100% deuterated NMP, one recovers approximately the scattering patterns observed for 80% deuterated NMP solutions.

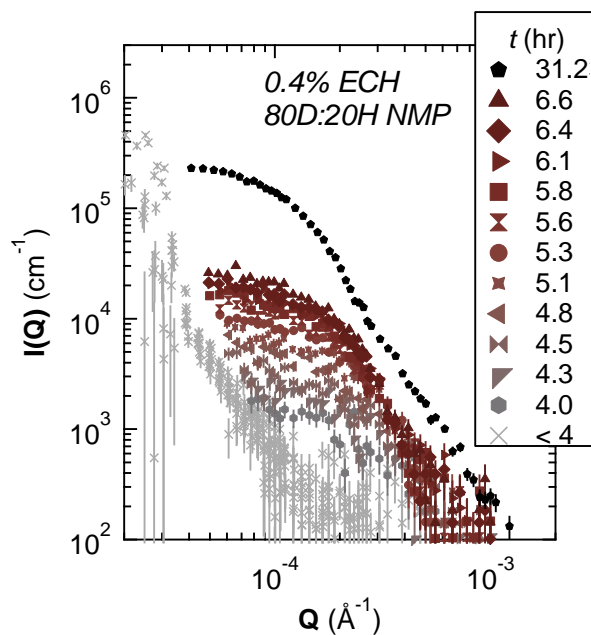




**Figure C.1:** SANS of PVDF and PEI solutions, in pure NMP- $d_9$  and in a mixture of 20% hydrogenous NMP + 80% NMP- $d_9$ . The shift in scattering between the two solvent systems for each polymer can be accounted for by the contrast variation and  $Q$ -independent incoherent scattering of  $0.33 \text{ cm}^{-1}$ .

## C.2 Time-resolved USANS Spectra
















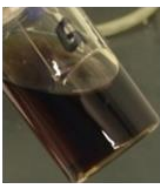


Several time-resolved USANS measurements from the 2019 experiment exhibited power law scattering at low- $Q$  which persisted for several hours (**Fig. C.2**). We attribute this unexpected power law to be an artefact from the banjo cell which becomes negligible after the sample begins to phase separate and generate appreciable scattering. The short-time anomalous scattering does not affect the time dependence of  $Q_K$  or  $I(Q_K)$ .



**Figure C.2:** Early stage of phase separation for a PEI-microgel casting solution containing 0.4% epichlorohydrin (ECH) in 80% deuterated solvent. The final equilibrated structure is also shown,  $t = 31.2$  hr. For  $t < 4$  hr., power law scattering was observed, which we attribute to the banjo cell.

### C.3 Visual evaluation of casting solutions

To further understand the interactions between PVDF and PEI in the absence of crosslinker epichlorohydrin (ECH), we varied the combination and order of addition of the other three components of mixed-matrix polymeric-particle (M2P2) casting solutions: PVDF, PEI, and hydrochloric acid (**Fig. C.3**).

Sample	Mixing time				
		19 min	27 min	53 min	73 min
I					
II	17 min	30 min	50 min	71 min	
					
III	10 min	17 min	30 min	44 min	65 min
					
IV	5 min	14 min	29 min	49 min	78 min
					

**Figure C.3:** Progression of color and turbidity change for mixtures of 7.5 wt% PEI, 11 wt% PVDF, and 0.12 wt% HCl in NMP. All samples kept at 80°C. **I:** PVDF + HCl, no PEI. **II:** PVDF + PEI, no HCl. **III:** PVDF + HCl + PEI. HCl was added to PVDF/NMP solution 14 min. prior to adding PEI. Mixing time is referenced to the addition of HCl. **IV:** PVDF + PEI + HCl. PEI and PVDF were combined 15 min. before the addition of HCl. Mixing time is referenced to the addition of HCl.

## BIBLIOGRAPHY

- (1) Güler, E.; Elizen, R.; Vermaas, D. A.; Saakes, M.; Nijmeijer, K. Performance-Determining Membrane Properties in Reverse Electrodialysis. *Journal of Membrane Science* **2013**, *446*, 266–276. <https://doi.org/10.1016/j.memsci.2013.06.045>.
- (2) Güler, E.; Elizen, R.; Saakes, M.; Nijmeijer, K. Micro-Structured Membranes for Electricity Generation by Reverse Electrodialysis. *Journal of Membrane Science* **2014**, *458*, 136–148. <https://doi.org/10.1016/j.memsci.2014.01.060>.
- (3) Hong, J. G.; Chen, Y. Nanocomposite Reverse Electrodialysis (RED) Ion-Exchange Membranes for Salinity Gradient Power Generation. *Journal of Membrane Science* **2014**, *460*, 139–147. <https://doi.org/10.1016/j.memsci.2014.02.027>.
- (4) Tedesco, M.; Scalici, C.; Vaccari, D.; Cipollina, A.; Tamburini, A.; Micale, G. Performance of the First Reverse Electrodialysis Pilot Plant for Power Production from Saline Waters and Concentrated Brines. *Journal of Membrane Science* **2016**, *500*, 33–45. <https://doi.org/10.1016/j.memsci.2015.10.057>.
- (5) Choi, S.; Chang, B.; Kang, J. H.; Diallo, M. S.; Choi, J. W. Energy-Efficient Hybrid FCDF-NF Desalination Process with Tunable Salt Rejection and High Water Recovery. *Journal of Membrane Science* **2017**, *541*, 580–586. <https://doi.org/10.1016/j.memsci.2017.07.043>.
- (6) Elimelech, M.; Phillip, W. A. The Future of Seawater Desalination: Energy, Technology, and the Environment. *Science* **2011**, *333* (6043), 712–717. <https://doi.org/10.1126/science.1200488>.
- (7) Werber, J. R.; Osuji, C. O.; Elimelech, M. Materials for Next-Generation Desalination and Water Purification Membranes. *Nat Rev Mater* **2016**, *1* (5), 16018. <https://doi.org/10.1038/natrevmats.2016.18>.
- (8) Sagle, A.; Freeman, B. Fundamentals of Membranes for Water Treatment. 17.
- (9) Geise, G. M.; Lee, H.-S.; Miller, D. J.; Freeman, B. D.; McGrath, J. E.; Paul, D. R. Water Purification by Membranes: The Role of Polymer Science. *J. Polym. Sci. B Polym. Phys.* **2010**, *48* (15), 1685–1718. <https://doi.org/10.1002/polb.22037>.
- (10) Lee, K. P.; Arnot, T. C.; Mattia, D. A Review of Reverse Osmosis Membrane Materials for Desalination—Development to Date and Future Potential. *Journal of Membrane Science* **2011**, *370* (1–2), 1–22. <https://doi.org/10.1016/j.memsci.2010.12.036>.

- (11) Asatekin, A.; Menniti, A.; Kang, S.; Elimelech, M.; Morgenroth, E.; Mayes, A. M. Antifouling Nanofiltration Membranes for Membrane Bioreactors from Self-Assembling Graft Copolymers. *Journal of Membrane Science* **2006**, *285* (1–2), 81–89. <https://doi.org/10.1016/j.memsci.2006.07.042>.
- (12) Petzetakis, N.; Doherty, C. M.; Thornton, A. W.; Chen, X. C.; Cotanda, P.; Hill, A. J.; Balsara, N. P. Membranes with Artificial Free-Volume for Biofuel Production. *Nat Commun* **2015**, *6* (1), 7529. <https://doi.org/10.1038/ncomms8529>.
- (13) Alsvik, I.; Hägg, M.-B. Pressure Retarded Osmosis and Forward Osmosis Membranes: Materials and Methods. *Polymers* **2013**, *5* (1), 303–327. <https://doi.org/10.3390/polym5010303>.
- (14) Chen, Q. P-Cyclodextrin Cation Exchange Polymer Membrane for Improved Second-Generation Glucose Biosensors. *Analytica Chimica Acta* **1995**, *8*.
- (15) Eisaman, M. D.; Parajuly, K.; Tuganov, A.; Eldershaw, C.; Chang, N.; Littau, K. A. CO<sub>2</sub> Extraction from Seawater Using Bipolar Membrane Electrodialysis. *Energy Environ. Sci.* **2012**, *5* (6), 7346. <https://doi.org/10.1039/c2ee03393c>.
- (16) Abdullah, S. Z.; Bérubé, P. R.; Horne, D. J. SEM Imaging of Membranes: Importance of Sample Preparation and Imaging Parameters. *Journal of Membrane Science* **2014**, *463*, 113–125. <https://doi.org/10.1016/j.memsci.2014.03.048>.
- (17) Tanaka, Y.; Ehara, R.; Itoi, S.; Goto, T. Ion-Exchange Membrane Electrodialytic Salt Production Using Brine Discharged from a Reverse Osmosis Seawater Desalination Plant. *Journal of Membrane Science* **2003**, *222* (1–2), 71–86. [https://doi.org/10.1016/S0376-7388\(03\)00217-5](https://doi.org/10.1016/S0376-7388(03)00217-5).
- (18) Diallo, M. S.; Kotte, M. R.; Cho, M. Mining Critical Metals and Elements from Seawater: Opportunities and Challenges. *Environ. Sci. Technol.* **2015**, *49* (16), 9390–9399. <https://doi.org/10.1021/acs.est.5b00463>.
- (19) Zhang, Q.; Vecitis, C. D. Conductive CNT-PVDF Membrane for Capacitive Organic Fouling Reduction. *Journal of Membrane Science* **2014**, *459*, 143–156. <https://doi.org/10.1016/j.memsci.2014.02.017>.
- (20) Donald, A. Phase Diagrams and Phase Separation. *Phase Diagrams* 37.
- (21) Kotte, M. R.; Cho, M.; Diallo, M. S. A Facile Route to the Preparation of Mixed Matrix Polyvinylidene Fluoride Membranes with In-Situ Generated Polyethyleneimine Particles. *Journal of Membrane Science* **2014**, *450*, 93–102. <https://doi.org/10.1016/j.memsci.2013.08.025>.

- (22) Rao Kotte, M.; Hwang, T.; Han, J.-I.; Diallo, M. S. A One-Pot Method for the Preparation of Mixed Matrix Polyvinylidene Fluoride Membranes with in Situ Synthesized and PEGylated Polyethyleneimine Particles. *Journal of Membrane Science* **2015**, *474*, 277–287. <https://doi.org/10.1016/j.memsci.2014.09.044>.
- (23) Hwang, T.; Kotte, M. R.; Han, J.-I.; Oh, Y.-K.; Diallo, M. S. Microalgae Recovery by Ultrafiltration Using Novel Fouling-Resistant PVDF Membranes with in Situ PEGylated Polyethyleneimine Particles. *Water Research* **2015**, *73*, 181–192. <https://doi.org/10.1016/j.watres.2014.12.002>.
- (24) Kotte, M. R.; Kuvarega, A. T.; Cho, M.; Mamba, B. B.; Diallo, Mamadou. S. Mixed Matrix PVDF Membranes With in Situ Synthesized PAMAM Dendrimer-Like Particles: A New Class of Sorbents for Cu(II) Recovery from Aqueous Solutions by Ultrafiltration. *Environ. Sci. Technol.* **2015**, *49* (16), 9431–9442. <https://doi.org/10.1021/acs.est.5b01594>.
- (25) Kotte, M. R.; Kuvarega, A. T.; Talapaneni, S. N.; Cho, M.; Coskun, A.; Diallo, M. S. A Facile and Scalable Route to the Preparation of Catalytic Membranes with in Situ Synthesized Supramolecular Dendrimer Particle Hosts for Pt(0) Nanoparticles Using a Low-Generation PAMAM Dendrimer (G1-NH<sub>2</sub>) as Precursor. *ACS Appl. Mater. Interfaces* **2018**, *10* (39), 33238–33251. <https://doi.org/10.1021/acsami.8b11351>.
- (26) Diallo, M. S.; Christie, S.; Swaminathan, P.; Johnson, J. H.; Goddard, W. A. Dendrimer Enhanced Ultrafiltration. 1. Recovery of Cu(II) from Aqueous Solutions Using PAMAM Dendrimers with Ethylene Diamine Core and Terminal NH<sub>2</sub> Groups. *Environ. Sci. Technol.* **2005**, *39* (5), 1366–1377. <https://doi.org/10.1021/es048961r>.
- (27) Diallo, M. S.; Christie, S.; Swaminathan, P.; Balogh, L.; Shi, X.; Um, W.; Papelis, C.; Goddard, W. A.; Johnson, J. H. Dendritic Chelating Agents. 1. Cu(II) Binding to Ethylene Diamine Core Poly(Amidoamine) Dendrimers in Aqueous Solutions. *Langmuir* **2004**, *20* (7), 2640–2651. <https://doi.org/10.1021/la036108k>.
- (28) Diallo, M. S.; Falconer, K.; Johnson, J. H. Dendritic Anion Hosts: Perchlorate Uptake by G5-NH<sub>2</sub> Poly(Propyleneimine) Dendrimer in Water and Model Electrolyte Solutions. *Environ. Sci. Technol.* **2007**, *41* (18), 6521–6527. <https://doi.org/10.1021/es0710959>.
- (29) Maiti, P. K.; Çağın, T.; Wang, G.; Goddard, W. A. Structure of PAMAM Dendrimers: Generations 1 through 11. *Macromolecules* **2004**, *37* (16), 6236–6254. <https://doi.org/10.1021/ma035629b>.
- (30) *Dendrimers and Other Dendritic Polymers*; Fréchet, J. M. J., Tomalia, D. A., Eds.; Wiley series in polymer science; Wiley: Chichester ; New York, 2001.

- (31) Chen, D. P.; Yu, C.; Chang, C.-Y.; Wan, Y.; Frechet, J. M. J.; Goddard, W. A.; Diallo, M. S. Branched Polymeric Media: Perchlorate-Selective Resins from Hyperbranched Polyethyleneimine. *Environ. Sci. Technol.* **2012**, *46* (19), 10718–10726. <https://doi.org/10.1021/es301418j>.
- (32) Mishra, H.; Yu, C.; Chen, D. P.; Goddard, W. A.; Dalleska, N. F.; Hoffmann, M. R.; Diallo, M. S. Branched Polymeric Media: Boron-Chelating Resins from Hyperbranched Polyethylenimine. *Environ. Sci. Technol.* **2012**, *46* (16), 8998–9004. <https://doi.org/10.1021/es301518x>.
- (33) Knecht, M. R.; Weir, M. G.; Myers, V. S.; Pyrz, W. D.; Ye, H.; Petkov, V.; Buttrey, D. J.; Frenkel, A. I.; Crooks, R. M. Synthesis and Characterization of Pt Dendrimer-Encapsulated Nanoparticles: Effect of the Template on Nanoparticle Formation. *Chem. Mater.* **2008**, *20* (16), 5218–5228. <https://doi.org/10.1021/cm8004198>.
- (34) Myers, V. S.; Weir, M. G.; Carino, E. V.; Yancey, D. F.; Pande, S.; Crooks, R. M. Dendrimer-Encapsulated Nanoparticles: New Synthetic and Characterization Methods and Catalytic Applications. *Chem. Sci.* **2011**, *2* (9), 1632. <https://doi.org/10.1039/c1sc00256b>.
- (35) Ye, R.; Zhukhovitskiy, A. V.; Deraedt, C. V.; Toste, F. D.; Somorjai, G. A. Supported Dendrimer-Encapsulated Metal Clusters: Toward Heterogenizing Homogeneous Catalysts. *Acc. Chem. Res.* **2017**, *50* (8), 1894–1901. <https://doi.org/10.1021/acs.accounts.7b00232>.
- (36) Da Vela, S.; Braun, M. K.; Dörr, A.; Greco, A.; Möller, J.; Fu, Z.; Zhang, F.; Schreiber, F. Kinetics of Liquid–Liquid Phase Separation in Protein Solutions Exhibiting LCST Phase Behavior Studied by Time-Resolved USAXS and VSANS. *Soft Matter* **2016**, *12* (46), 9334–9341. <https://doi.org/10.1039/C6SM01837H>.
- (37) Barker, J. G.; Glinka, C. J.; Moyer, J. J.; Kim, M. H.; Drews, A. R.; Agamalian, M. Design and Performance of a Thermal-Neutron Double-Crystal Diffractometer for USANS at NIST. *J Appl Crystallogr* **2005**, *38* (6), 1004–1011. <https://doi.org/10.1107/S0021889805032103>.
- (38) Agamalian, M. II.1.3.1 Bonse-Hart USANS Instrument. In *Neutrons in Soft Matter*; John Wiley & Sons, Inc., 2011; pp 73–94.
- (39) Agamalian, M.; Wignall, G. D.; Triolo, R. Optimization of a Bonse–Hart Ultra-Small-Angle Neutron Scattering Facility by Elimination of the Rocking-Curve Wings. *J Appl Crystallogr* **1997**, *30* (3), 345–352. <https://doi.org/10.1107/S0021889896014343>.
- (40) Carpenter, J. M.; Agamalian, M. Aiming for the Theoretical Limit of Sensitivity of Bonse-Hart USANS Instruments. *J. Phys.: Conf. Ser.* **2010**, *251*, 012056. <https://doi.org/10.1088/1742-6596/251/1/012056>.
- (41) Kovési, P. Good Colour Maps: How to Design Them. *arXiv:1509.03700 [cs]* **2015**.

- (42) Barker, J. G.; Pedersen, J. S. Instrumental Smearing Effects in Radially Symmetric Small-Angle Neutron Scattering by Numerical and Analytical Methods. *J Appl Crystallogr* **1995**, *28* (2), 105–114. <https://doi.org/10.1107/S0021889894010095>.
- (43) Lake, J. A. An Iterative Method of Slit-Correcting Small Angle X-Ray Data. *Acta Cryst* **1967**, *23* (2), 191–194. <https://doi.org/10.1107/S0365110X67002440>.
- (44) Kline, S. R. Reduction and Analysis of SANS and USANS Data Using IGOR Pro. *J Appl Crystallogr* **2006**, *39* (6), 895–900. <https://doi.org/10.1107/S0021889806035059>.
- (45) Schelten, J.; Schmatz, W. Multiple-Scattering Treatment for Small-Angle Scattering Problems. *J Appl Crystallogr* **1980**, *13* (4), 385–390. <https://doi.org/10.1107/S0021889880012356>.
- (46) Dhont, J. K. G. Spinodal Decomposition Kinetics: The Initial and Intermediate Stages. In *Dynamics: Models and Kinetic Methods for Non-equilibrium Many Body Systems*; Karkheck, J., Ed.; Springer Netherlands: Dordrecht, 2000; pp 73–120. [https://doi.org/10.1007/978-94-011-4365-3\\_6](https://doi.org/10.1007/978-94-011-4365-3_6).
- (47) Takenaka, M.; Izumitani, T.; Hashimoto, T. Slow Spinodal Decomposition in Binary Liquid Mixtures of Polymers. 2. Effects of Molecular Weight and Transport Mechanism. *Macromolecules* **1987**, *20* (9), 2257–2264. <https://doi.org/10.1021/ma00175a034>.
- (48) Wang, Z.-Y.; Konno, M.; Saito, S. Theoretical Study of Spinodal Decomposition at Intermediate Stages. *Phys. Rev. A* **1991**, *44* (8), 5058–5063. <https://doi.org/10.1103/PhysRevA.44.5058>.
- (49) Lefebvre, A. A.; Lee, J. H.; Balsara, N. P.; Hammouda, B. Fluctuations in Highly Metastable Polymer Blends. 5.
- (50) Nedoma, A. J.; Lai, P.; Jackson, A.; Robertson, M. L.; Wanakule, N. S.; Balsara, N. P. Phase Diagrams of Blends of Polyisobutylene and Deuterated Polybutadiene as a Function of Chain Length. *Macromolecules* **2011**, *44* (8), 3077–3084. <https://doi.org/10.1021/ma200258w>.
- (51) Hammouda, B. PROBING NANOSCALE STRUCTURES – THE SANS TOOLBOX. 692.
- (52) Hester, J. F.; Banerjee, P.; Won, Y.-Y.; Akthakul, A.; Acar, M. H.; Mayes, A. M. ATRP of Amphiphilic Graft Copolymers Based on PVDF and Their Use as Membrane Additives. *Macromolecules* **2002**, *35* (20), 7652–7661. <https://doi.org/10.1021/ma0122270>.
- (53) Li, Q.; Lin, H.-H.; Wang, X.-L. Preparation of Sulfobetaine-Grafted PVDF Hollow Fiber Membranes with a Stably Anti-Protein-Fouling Performance. *Membranes* **2014**, *4* (2), 181–199. <https://doi.org/10.3390/membranes4020181>.



- (54) Taguet, A.; Sauguet, L.; Ameduri, B.; Boutevin, B. Fluorinated Cotelomers Based on Vinylidene Fluoride (VDF) and Hexafluoropropene (HFP): Synthesis, Dehydrofluorination and Grafting by Amine Containing an Aromatic Ring. *Journal of Fluorine Chemistry* **2007**, *128* (6), 619–630. <https://doi.org/10.1016/j.jfluchem.2007.02.005>.
- (55) Bhatia, S.; Barker, J.; Mourchid, A. Scattering of Disklike Particle Suspensions: Evidence for Repulsive Interactions and Large Length Scale Structure from Static Light Scattering and Ultra-Small-Angle Neutron Scattering. *Langmuir* **2003**, *19* (3), 532–535. <https://doi.org/10.1021/la0265732>.
- (56) Wanakule, N. S.; Nedoma, A. J.; Robertson, M. L.; Fang, Z.; Jackson, A.; Garetz, B. A.; Balsara, N. P. Characterization of Micron-Sized Periodic Structures in Multicomponent Polymer Blends by Ultra-Small-Angle Neutron Scattering and Optical Microscopy. *Macromolecules* **2008**, *41* (2), 471–477. <https://doi.org/10.1021/ma701922y>.
- (57) Bahadur, J.; Radlinski, A.; Melnichenko, Y. B.; Mastalerz, M. SANS/USANS Study of the New Albany Shale: A Treatise on Microporosity. 35.
- (58) Bahadur, J.; Radlinski, A. P.; Melnichenko, Y. B.; Mastalerz, M.; Schimmelmann, A. Small-Angle and Ultrasmall-Angle Neutron Scattering (SANS/USANS) Study of New Albany Shale: A Treatise on Microporosity. *Energy Fuels* **2015**, *29* (2), 567–576. <https://doi.org/10.1021/ef502211w>.
- (59) Schaefer, D. W.; Agamalian, M. M. Ultra-Small-Angle Neutron Scattering: A New Tool for Materials Research. *Current Opinion in Solid State and Materials Science* **2004**, *8* (1), 39–47. <https://doi.org/10.1016/j.cossms.2004.01.012>.
- (60) Chen, W.-R.; Iwashita, T.; Porcar, L.; Wang, Z.; Wang, Y.; Sánchez-Díaz, L. E.; Hamilton, W. A.; Egami, T. Origin of Nonlinear Rheology in Interacting Colloidal Suspensions. 24.
- (61) Lee Perry, W.; Clements, B.; Ma, X.; Mang, J. T. Relating Microstructure, Temperature, and Chemistry to Explosive Ignition and Shock Sensitivity. *Combustion and Flame* **2018**, *190*, 171–176. <https://doi.org/10.1016/j.combustflame.2017.11.017>.
- (62) Mueller, E.; Alsop, R. J.; Scotti, A.; Bleuel, M.; Rheinstädter, M. C.; Richtering, W.; Hoare, T. Dynamically Cross-Linked Self-Assembled Thermoresponsive Microgels with Homogeneous Internal Structures. *Langmuir* **2018**, *34* (4), 1601–1612. <https://doi.org/10.1021/acs.langmuir.7b03664>.
- (63) Da Vela, S.; Exner, C.; Schäufele, R. S.; Möller, J.; Fu, Z.; Zhang, F.; Schreiber, F. Arrested and Temporarily Arrested States in a Protein–Polymer Mixture Studied by USAXS and VSANS. *Soft Matter* **2017**, *13* (46), 8756–8765. <https://doi.org/10.1039/C7SM01434A>.

- (64) Yang, J.; Hong, K.; Bonnesen, P. V. Synthesis of N1-tritylethane-1,1,2,2-d4-1,2-diamine: A Novel Mono-protected C-deuterated Ethylenediamine Synthon. *Journal of Labelled Compounds and Radiopharmaceuticals* **2012**, *55* (13), 463–466. <https://doi.org/10.1002/jlcr.2977>.
- (65) Pynn, R. Neutron Scattering—A Non-Destructive Microscope for Seeing Inside Matter. In *Neutron Applications in Earth, Energy and Environmental Sciences*; Liang, L., Rinaldi, R., Schober, H., Eds.; Anderson, I. S., Hurd, A. J., McGreevy, R. L., Series Eds.; Neutron Scattering Applications and Techniques; Springer US: Boston, MA, 2009; pp 15–36. [https://doi.org/10.1007/978-0-387-09416-8\\_2](https://doi.org/10.1007/978-0-387-09416-8_2).
- (66) Ford, R. R. Collection of Python Scripts Used to Reduce and Analyze USANS Data. April 19, 2021. [dx.doi.org/10.22002/D1.1954](https://doi.org/10.22002/D1.1954).
- (67) *Mathematical Optimization Techniques*; Richard Bellman, Ed.; University of California Press, 1963.

